SANDIA REPORT

SAND2009-7034
Unlimited Release
Printed January 2010

Studies on Metal-Dielectric Plasmonic Structures

Mark D. Thoreson, Zhengtong Liu, Uday K. Chettiar, Piotr Nyga,
Alexander V. Kildishev, Vladimir P. Drachev, Michael V. Pack (Org. 1128)
and Vladimir M. Shalaev

Prepared by
Sandia National Laboratories
Albuquerque, New Mexico 87185 and Livermore, California 94550

Sandia is a multiprogram laboratory operated by Sandia Corporation,
a Lockheed Martin Company, for the United States Department of Energy's
National Nuclear Security Administration under Contract DE-AC04-94-AL85000.

Issued by Sandia National Laboratories, operated for the United States Department of Energy by Sandia Corporation.

Available to DOE and DOE contractors from
U.S. Department of Energy
Office of Scientific and Technical Information
P.O. Box 62
Oak Ridge, TN 37831

Telephone: (865) 576-8401
Facsimile: (865) 576-5728
E-Mail: reports@adonis.osti.gov
Online ordering: http://www.osti.gov/bridge

Available to the public from
U.S. Department of Commerce
National Technical Information Service
5285 Port Royal Rd
Springfield, VA 22161

Telephone: (800) 553-6847
Facsimile: (703) 605-6900
E-Mail: orders@ntis.fedworld.gov
Online ordering: http://www.ntis.gov/help/ordermethods.asp?loc=7-4-0#online

SAND2009-7034
Unlimited Release
Printed January 2010

Studies on Metal-Dielectric Plasmonic Structures

Mark D. Thoreson, Zhengtong Liu, Uday K. Chettiar, Piotr Nyga,
Alexander V. Kildishev, Vladimir P. Drachev and V. M. Shalaev
Birck Nanotechnology Center
Purdue University
1205 West State Street
West Lafayette, IN
mthoreso@purdue.edu

Michael V. Pack (Org. 1128)
Sandia National Laboritories
PO Box 5800
Mail Stop 1423
Albuquerque, NM 87185-1423

Abstract

The interaction of light with nanostructured metal leads to a number of fascinating phenomena, including plasmon oscillations that can be harnessed for a variety of cutting-edge applications. Plasmon oscillation modes are the collective oscillation of free electrons in metals under incident light. Previously, surface plasmon modes have been used for communication, sensing, nonlinear optics and novel physics studies. In this report, we describe the scientific research completed on metal-dielectric plasmonic films accomplished during a multi-year Purdue Excellence in Science and Engineering Graduate Fellowship sponsored by Sandia National Laboratories. A variety of plasmonic structures, from random 2D metal-dielectric films to 3D composite metal-dielectric films, have been studied in this research for applications such as surface-enhanced Raman sensing, tunable superlenses with resolutions beyond the diffraction limit, enhanced molecular absorption, infrared obscurants, and other real-world applications.

Contents

List of Figures

List of Tables

Chapter 1

Introduction

This is a review of research performed through the Purdue Excellence in Science and Engineering Fellowship sponsored by Sandia National Laboratories. The studies detailed in this document have been performed at Purdue University in the Photonics and Spectroscopy Lab, headed by Prof. Vladimir M. Shalaev, and at the Scifres Nanofabrication Laboratory at the Birck Nanotechnology Center. This document is laid out in several sections, each corresponding to a group of related research and projects. A brief overview of plasmonics and plasmon excitation is provided first. We next describe results from semicontinuous, single-layer metal films. Next, the research peformed on multilayer films is detailed. Finally, we end with a section on the simulation of our plasmonic structures.

At the heart of the research performed through this fellowship is the study of plasmonics and the coupling of light to surface modes in a metal. The interaction of light with metal is often complicated and useful, as we shall see in the following chapters. In the vast literature on plasmonics, devices that support plasmon oscillations have been engineered for a wide variety of purposes. As an example of the importance of understanding the physics of plasmonics and applications of plasmonic devices, the journal *Plasmonics* is devoted solely to this very topic.

Plasmonic devices support the collective oscillation of conduction band electrons, called a plasmon, in a metal or metallic structure. When irradiated by light or electrons, the energy incident on a metallic structure can be absorbed by the metal's free electrons, causing these conduction band electrons to oscillate. This oscillation has a resonant nature such that incident light at the right frequency will experience large spectral absorption and a dip in reflection from the material. These resonance effects in reflection and absorption have been known for some time and were even naively used in Roman artwork and the stained glass windows of cathedrals in the Middle Ages. The resonance frequency of a plasmonic structure depends strongly on its constituent material and its morphology. Small metal spheres embedded in a dielectric host will absorb most strongly at a different frequency than nanoscale metal rods or bulk metal, for example. In order to create low-loss resonances in the optical range, noble metals such as gold or silver are usually used in plasmonics.

Metal-dielectric plasmonic structures have been applied successfully in a number of projects within our research at Purdue University. Further understanding of the nature of these materials and their optical properties has led to applications in a wide range of fields, such as biological and chemical agent sensing, infrared obscurants and filters, near-field superlenses that can image

objects smaller than the conventional lens wavelength limit, and even potential applications in negative-refraction metamaterials. In this work, we have studied these and other applications of metal-dielectric plasmonic structures.

Plasmonics and Plasmonic Structures

Plasmonics is at the core of this research. As such, it is necessary to review the major concepts of plasmons, plasmonics, and light-metal interactions. Still, we can ask a more fundamental and basic question of why study plasmonics at all? Our answer is that plasmonics, or more broadly the study of light and metal interactions and applications, is an extremely robust and useful research area. The area of plasmonics spans seemingly unrelated fields such as medicine (where plasmonics can be used for imaging [1] and gold nanoshells can be used in cancer treatment [2, 3], for example), alternative energy (light concentrators for photovoltaics [4]), integrated circuits (plasmonic interconnects [5]), and more. Plasmons can be used in such a wide array of applications in part because they are arise at the very basic level of light and matter interactions, just as traditional optics has been used in almost every aspect of scientific research.

The interaction of electromagnetic radiation with metal is desribed in elementary electromagnetic textbooks in a rather uninteresting way. It is often couched in terms of reflections from so-called perfect metals and the concepts surrounding the skin effect in good conductors. Although useful for instruction at the undergraduate level, these ideas lose their luster when the frequency of the incident radiation moves out of the radio-frequency range and into the much higher optical range. At frequencies in this regime, the interaction of radiation with real metals becomes much more interesting, and possibly very useful in applications. In a conductive metal, the electrons are not strongly attached to individual atomic nuclei and are free to move under the influence of an applied electric field. Researchers experimentally confirmed several decades ago that directing light at a metal/dielectric inteface can, under the right circumstances, induce a resonant interaction between the waves and the mobile electrons at the surface of the metal [6]. In other words, the oscillations of electrons at the surface can couple to those of the electromagnetic field outside the metal. The result is the generation of surface plasmons – density waves of electrons that propagate along the interface like the ripples that spread across the surface of a pond after a stone is thrown into the water.

To understand how light interacts with real metals, we need to know how the metal responds to electromagetic radiation. In elementary textbooks, a material's response is characterized by its electric permittivity ε and magnetic permeability μ. However, these values vary with frequency, and although experimental data is available for most materials (see, for instance, the paper by Johnson and Christy [7] or the handbook by Palik [8]), it is useful to have an analytical model that predicts the values of these parameters for any frequency. We next look at two such models, one built on the other, that can predict some important features of the optical properties of metals.

The Drude Model

The most commonly used model for metal permittivity is the classical Drude model, developed by Paul Drude in 1900 [9, 10, 11]. The model was derived in order to describe the electrical conduction properties of materials (particularly metals), and it predicts with reasonable accuracy the permittivity and conductivity of real metals by modeling the conduction-band electron motion

in a metal lattice under an applied electric field. The Drude model takes a macroscopic view of charge carrier (electron or hole) motion, using a simple equation of motion and deriving the material permittivity. In the Drude model, metals are characterized by a cloud of free electrons that are not bound to a particular atomic nucleus but are free to move about within the metal lattice. The model also includes frictional damping that describes the resistance to movement felt by the electrons. This damping arises from collisions within the lattice between the moving electrons and the positive, stationary ions. Although the Drude model does not take into account electron-electron interactions, it is still in surprisingly good agreement with the experimentally measured permittivity data for metals, particularly for the noble metals, in certain frequency ranges.

In terms of the dielectric permittivity, the Drude model is expressed as

$$\varepsilon = 1 - \frac{\omega_p^2}{\omega^2 + i\omega\Gamma_p}, \tag{1.1}$$

where ω_p is the plasma frequency of the material (a constant for each material), Γ_p is the damping (or relaxation) rate, ω is the frequency of interest and i is the complex number, $i = \sqrt{-1}$. The calculated values for the Drude model for silver and gold are summarized in Table 1.1.

Sometimes, the first term on the right side of Equation 1.1 is written in a different form to account for a background interband contribution to the permittivity. In this case, the '1' is replaced by ε_∞, a frequency-independent constant that describes the contribution to the permittivity from electron transitions from one electron band into another. Typically these transitions occur from the *d* band of the metal and act to red-shift the plasmon excitation resonance wavelength of the metal [12]. These interband transitions do depend on the frequency of radiation, of course, but for narrow ranges of interest away from interband resonances, the ε_∞ notation can be adequate. Electronic interband transitions influence the surface plasmon resonance in metallic nanoparticles significantly. Taking into account the interband transitions in the dielectric function, Ref. [13] provides a nice derivation for the resonance frequency, the bandwidth and the maximum of the light absorption cross section of noble metal nanoparticles.

Nearly all of the studies described in this document relate to experiments with silver, with a few using gold. Therefore, the commplex permittivities of gold and silver are shown below. The permittivity presented include the analytical Drude model, the analytical Drude-Lorentz model, and the generally accepted experimental data for bulk metals. The experimental data are taken from widely cited paper by Johnson and Christy published in 1972 concerning measured (bulk) material permittivity values [7]. Note that these experimental values are only valid for bulk silver and gold; the values can actually vary for nanoscale systems, as has been shown by Drachev *et al.* [14] and other researchers.

The Drude-Lorentz Model

The Drude model can be extended to more closely match experimental data by adding frequency-dependent contributions from interband transitions. If the frequency-dependent nature of the inter-

Table 1.1. Drude model parameters for silver and gold (From [7]).

Metal	Plasma Frequency	Damping Factor
	(ω_p, eV)	(Γ_p, eV)
Silver (Ag)	9.176	0.021
Gold (Au)	9.062	0.070

band transitions is important in an analysis of the permittivity of a metal, Lorentz oscillation terms can be added to the Drude model in order to provide a more accurate prediction of the permittivity. The Lorentz terms model the bound charges in the metal through harmonic (Lorentz) oscillators. With a single Lorentz resonant term, the Drude-Lorentz expression for permittivity is

$$\varepsilon = \varepsilon_\infty - \frac{\omega_p^2}{\omega^2 + i\Gamma_p\omega} - \frac{f_1\omega_1^2}{\omega^2 - \omega_1^2 + i\Gamma_1\omega}.$$

As with the Drude model, ω_p is the plasma frequency of the material, Γ_p is the relaxation rate, ω is the frequency of interest and i is the complex number, $i = \sqrt{-1}$. The new Lorentz term includes the Lorentz oscillator damping rate Γ_1, the Lorentz resonance width ω_1 and a weighting factor f_1. With multiple Lorentz terms, the expression can be extended to [15]

$$\varepsilon = \varepsilon_\infty - \frac{\omega_p^2}{\omega^2 + i\Gamma_p\omega} - \sum \frac{f_n\omega_n^2}{\omega^2 - \omega_n^2 + i\Gamma_n\omega}.$$

In this form, the contribution from interband transitions at infinte frequency (that is, the static contribution) is ε_∞. The Drude-Lorentz model parameters for silver and gold assuming a single Lorentz oscillator term are shown in Table 1.2. The addition of several oscillator terms to the permittivity function further increases the fit to experimental data, but it also increases the complexity of calculations involving the permittivity function. Drude-Lorentz models with multiple oscillator terms can be found in a variety of textbooks or in the published literature. One recommended source for modeling information is the Purdue University NanoHub online computational initiative [16], which provides a very useful tool called PhotonicsDB where material parameters and models for a variety of materials are available [17].

Plasmon Excitation / Resonance Condition

The energy absorbed by metals like silver and gold from an incident electromagnetic field is not lost, of course. The energy has to go somewhere, and due to coupling between the charged free particles in a metal (electrons) and the electromagnetic field, the energy goes into moving the electrons, causing them to oscillate in unison with the applied electric field. This collective

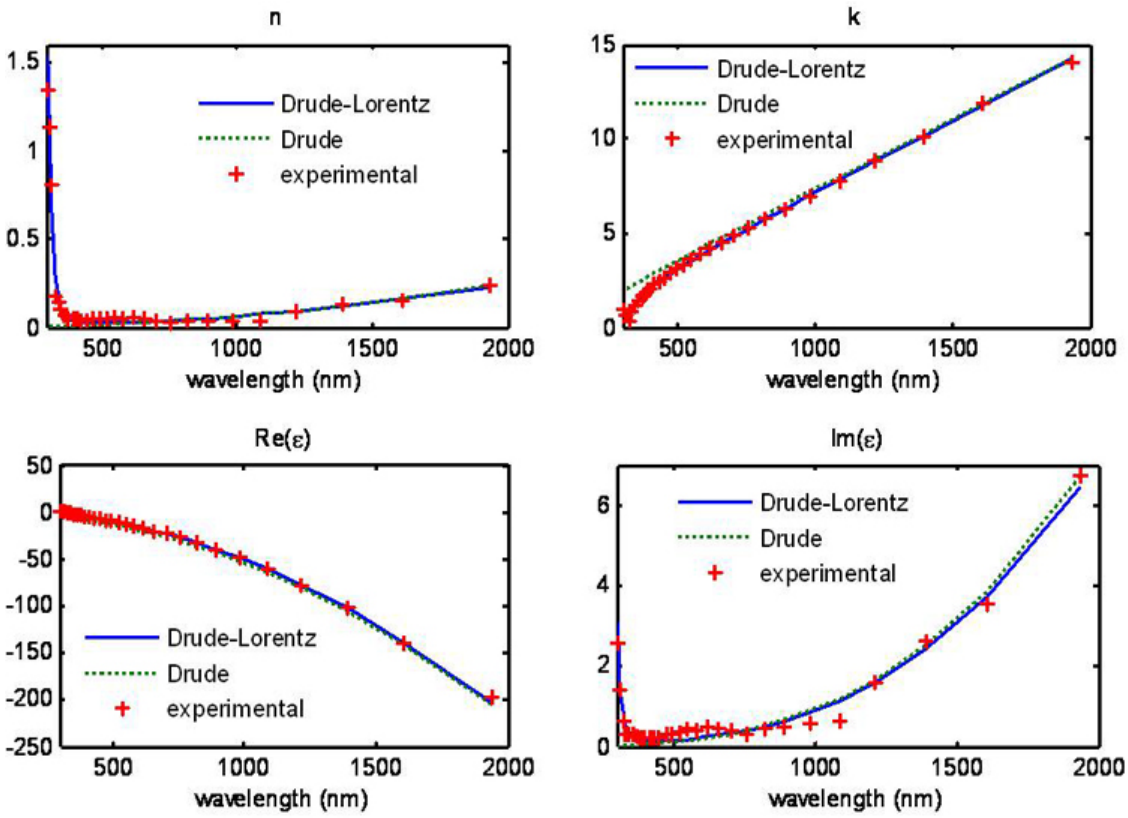

Figure 1.1. Silver (Ag) complex refractive index and complex permittivity from the analytical Drude model (dashed lines), the analytical Drude-Lorentz model (solid lines) and experimentally obtained data (data points, from [7]). (Courtesy of Z. Liu)

Table 1.2. Drude-Lorentz model parameters for silver and gold with one Lorentz oscillation term (From [7]).

Metal	ε_∞	Plasma Freq. (ω_p, eV)	Plasma Relaxation (Γ_p, eV)	Lorentz Freq. (ω_1, eV)	Weighting Factor (f_1)	Lorentz Relaxation (Γ_1, eV)
Silver (Ag)	3.7180	9.2093	0.0200	4.2840	0.4242	0.3430
Gold (Au)	6.8890	8.9601	0.0723	2.9715	1.7857	0.9503

electron oscillation, known as a plasmon, is oscillation of the electron gas (or plasma) surrounding the atomic lattice sites of a metal. When plasmons couple with a photon, the resulting quasi-particle is called a polariton. This polariton propagates along the surface of the metal until it decays, either by absorption, whereupon the energy is converted into phonons, or by a radiative transition into a photon. When plasmons are excited at an interface of metal, they are known as surface plasmons. The frequency of plasmon excitation is very dependent on the metal properties and the geometry under consideration [18]. That is, bulk metal plasmon excitation occurs at a different incident frequency than for a film of metal interfacing a dielectric. If the metal is spherical or some other shape embedded in a dieletric, the frequency of plasmon oscillation will again be different. For even more complicated systems, such as self-affine or fractal-type metallic structures commonly used in our research, a large number of surface plasmon modes can be excited (corresponding to different frequencies). This results in a very broad absorption band that extends from the bulk plasmon frequency and into the longer wavelengths [19, 20].

Mathematically, the excitation of surface plasmons involves the match of transverse wavevectors between the incident light and the surface plasmon mode at the interface. We review here the mathematics of surface plasmon modes, following closely the derivation by Raether [21]. Other work on surface plasmons is easily found both in texts [19, 22, 23] and in myriad publications in the literature.

Surface plasmons can be excited by both electrons and photons. Surface plasmon excitation by electrons is created rather simply, by directing energetic electrons into a metal. As the electrons scatter, energy is transferred into the plasma. The component of the scattering vector parallel to the surface results in the formation of a surface plasmon.

Excitation of a plasmon by photons is more complicated, and requires the use of a coupling method such as an intermediate medium (a prism, for instance) or a grating in order to match the photon and surface plasmon wave vectors. A prism can be positioned against a thin metal film in the Kretschmann configuration or very close to a metal surface in the Otto configuration [18]. A grating coupler matches the wave vectors by increasing the incident wave vector by the spatial frequency of the grating. This method, while less frequently utilized, is critical to the theoretical understanding of the impact of surface roughness.

The analysis begins by writing the electric field of a propagating electromagnetic wave, which

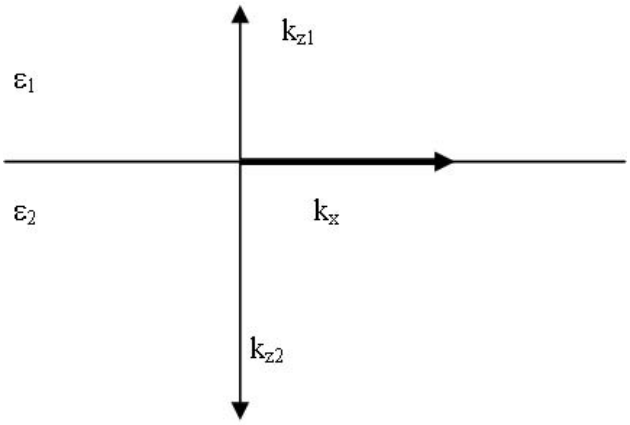

Figure 1.2. Coordinate system for surface plasmons at an infinite plane surface.

can be expressed as

$$E = E_0 \exp[i(k_x x + k_z z - \omega t)], \tag{1.2}$$

where k is the wave number and ω is the frequency of the wave. By solving Maxwell's equations for the electromagnetic wave at an interface between two materials with relative dielectric constants ε_1 and ε_2 (see Figure 1.2) and with the appropriate continuity relationships, the boundary conditions at the interface are found to be [21]

$$\frac{k_{z1}}{\varepsilon_1} + \frac{k_{z2}}{\varepsilon_2} = 0 \tag{1.3}$$

and

$$k_x^2 + k_{zi}^2 = \varepsilon_i \left(\frac{\omega}{c}\right)^2 \qquad i = 1,2 \tag{1.4}$$

where c is the speed of light in a vacuum. Solving these two equations, the dispersion relationship for a wave propagating on the surface is

$$k_x = \frac{\omega}{c}\left(\frac{\varepsilon_1 \varepsilon_2}{\varepsilon_1 + \varepsilon_2}\right)^{1/2}. \tag{1.5}$$

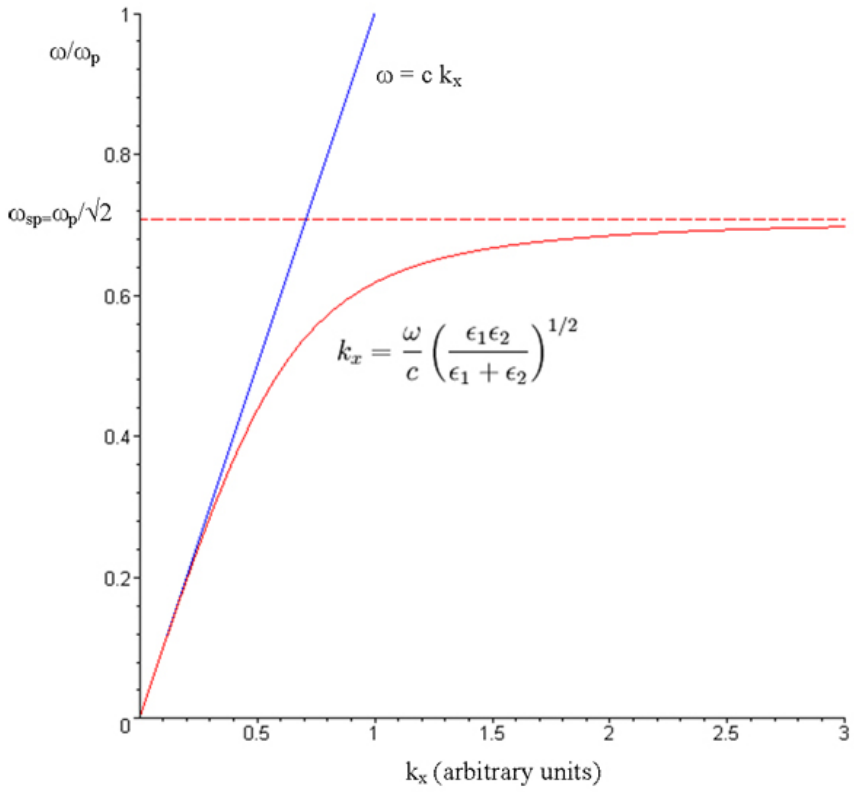

Figure 1.3. Surface plasmon dispersion relationship. At low wavenumbers, the surface plasmon curve approaches the propagating free-space curve.

In the free electron model of an electron gas (that is, ignoring damping collisions described by Γ), the permittivity is [24]

$$\varepsilon(\omega) = 1 - \frac{\omega_P^2}{\omega^2}, \tag{1.6}$$

where the plasma frequency is

$$\omega_P = \sqrt{\frac{4\pi N e^2}{m^*}}. \tag{1.7}$$

Here N is the electron density, e is the charge of the electron, and m^* is the effective mass of the electron. Note that, as mentioned before, the plasma frequency is a constant for each material. The dispersion relationship is plotted in Figure 1.3. At low k, the surface plasmon behaves like a photon, but as k increases, the dispersion relationship bends over and reaches an asymptotic limit. Since the dispersion curve lies to the right of the light curve, $\omega = ck_x$, the surface plasmon is non-radiative. Finally, solving these equations gives us the maximum frequency of the surface plasmon

$$\omega_{SP} = \omega_P / \sqrt{1+\varepsilon_2}. \tag{1.8}$$

In the case of air, this result simplifies to

$$\omega_{SP} = \omega_P / \sqrt{2}. \tag{1.9}$$

If we assume that ε_2 is real and $\varepsilon_2 > 0$, then it must be true that $\varepsilon_1 < 0$, a condition which is satisfied in metals. Electromagnetic waves passing through a metal experience damping due to electrical conductivity and electron-core interactions. These effects show up in as an imaginary component of the dielectric function. The dielectric function of a metal is expressed $\varepsilon_1 = \varepsilon_1' + i\varepsilon_1''$ where ε_1' and ε_1'' are the real and imaginary parts of the dielectric function, respectively. Generally $|\varepsilon_1'| \gg \varepsilon_1''$ so the wavenumber can be expressed in terms of its real and imaginary components [21]

$$k_x = k_x' + ik_x'' = \left[\frac{\omega}{c}\left(\frac{\varepsilon_1'\varepsilon_2}{\varepsilon_1'+\varepsilon_2}\right)^{1/2}\right] + i\left[\frac{\omega}{c}\left(\frac{\varepsilon_1'\varepsilon_2}{\varepsilon_1'+\varepsilon_2}\right)^{3/2}\frac{\varepsilon_1''}{2(\varepsilon_1')^2}\right]. \tag{1.10}$$

The wave vector gives us insight into physically meaningful properties of the electromagnetic wave such as its spatial extent and coupling requirements for wave vector matching.

As a surface plasmon propagates along the surface, it quickly loses its energy to the metal due to absorption. The intensity of the surface plasmon decays with the square of the electric field, so

at a distance x, the intensity has decreased by a factor of $e^{(-2k_x x)}$. The propagation length is defined as the distance for the surface plasmon to decay by a factor of $1/e$. This condition is satisfied at a length [25]

$$L = \frac{1}{2k_x''}. \tag{1.11}$$

Likewise, the electric field falls off exponentially normal to the surface. The skin depth is defined as the distance where the electric field falls off by $1/e$. The field will decay at different rates in the metal and dielectric medium, and the skin depth in each medium can be expressed as [25]

$$z_i = \frac{\lambda}{2\pi}\left(\frac{|\varepsilon_1'| + \varepsilon_2}{\varepsilon_i^2}\right)^{1/2} \tag{1.12}$$

where i indicates the medium of propagation. Surface plasmons are very sensitive to even slight perturbations in a surface within the skin depth; because of this, surface plasmons are often used to probe inhomogeneities of a surface.

Chapter 2

Single-Layer Semicontinuous Films

Fabrication and Characterization of Semicontinuous Metal Films

The resonance frequency of a plasmonic structure depends strongly on its constituent material and its morphology. The shape factor in the surface plasmon excitation mathematics [18] tells us that small metal spheres embedded in a dielectric host will absorb energy most strongly at a different frequency than nanoscale metal rods or bulk metal, for example. Plasmonic structures with a large number of random, fractal-like metallic structures will therefore exhibit resonances at a variety of frequencies, from the single-particle resonance in the UV to complex-shape resonances out into the mid-infrared range. Semicontinuous metal films have this fractal structure near the percolation threshhold [26, 27, 28, 20] and hence show broadband absorption [29, 30]. In our work, we typically use either silver or gold as the metal component in our films in order to create low-loss, resonant samples for the optical range. Silver and gold are often the metals of choice for plasmonic structures in general due to their low loss [14, 31].

Single-layer semicontinuous silver films were fabricated by various means for a number of research projects at Purdue. The two primary methods we used to fabricate semicontinuous metal films were electron-beam evaporation and pulsed laser deposition (PLD), both of which are physical vapor deposition processes [32]. For brevity, we describe only our results on e-beam evaporation. Numerous publications on PLD are available, such as the book by Chrisey [33].

Electron-Beam Evaporation

The semicontinuous silver films were most often fabricated on a dielectric substrate under vacuum evaporation with an electron beam physical vapor deposition system. This process involves the controlled deposition of silver and dielectric material onto an initial dielectric substrate. Standard microscope glass slides (Fisher Scientific) were cut into 25×25 mm sections for use as initial substrates. The cut slides were cleaned using several steps, including multiple solvent rinses, a piranha (H_2O_2:$3H_2SO_4$) acid bath, rinsing in ultrapure water (Birck Nanograde Water [34]) and drying with dry gaseous nitrogen. Silver shot source material (Alfa Aesar, 99.9999% purity, 1-3 mm diameter) and SiO_2 pellets (Kurt J. Lesker Corp., 99.995% purity, cut quartz) were used for physical vapor deposition of the films onto the glass substrates. Thin-film deposition was per-

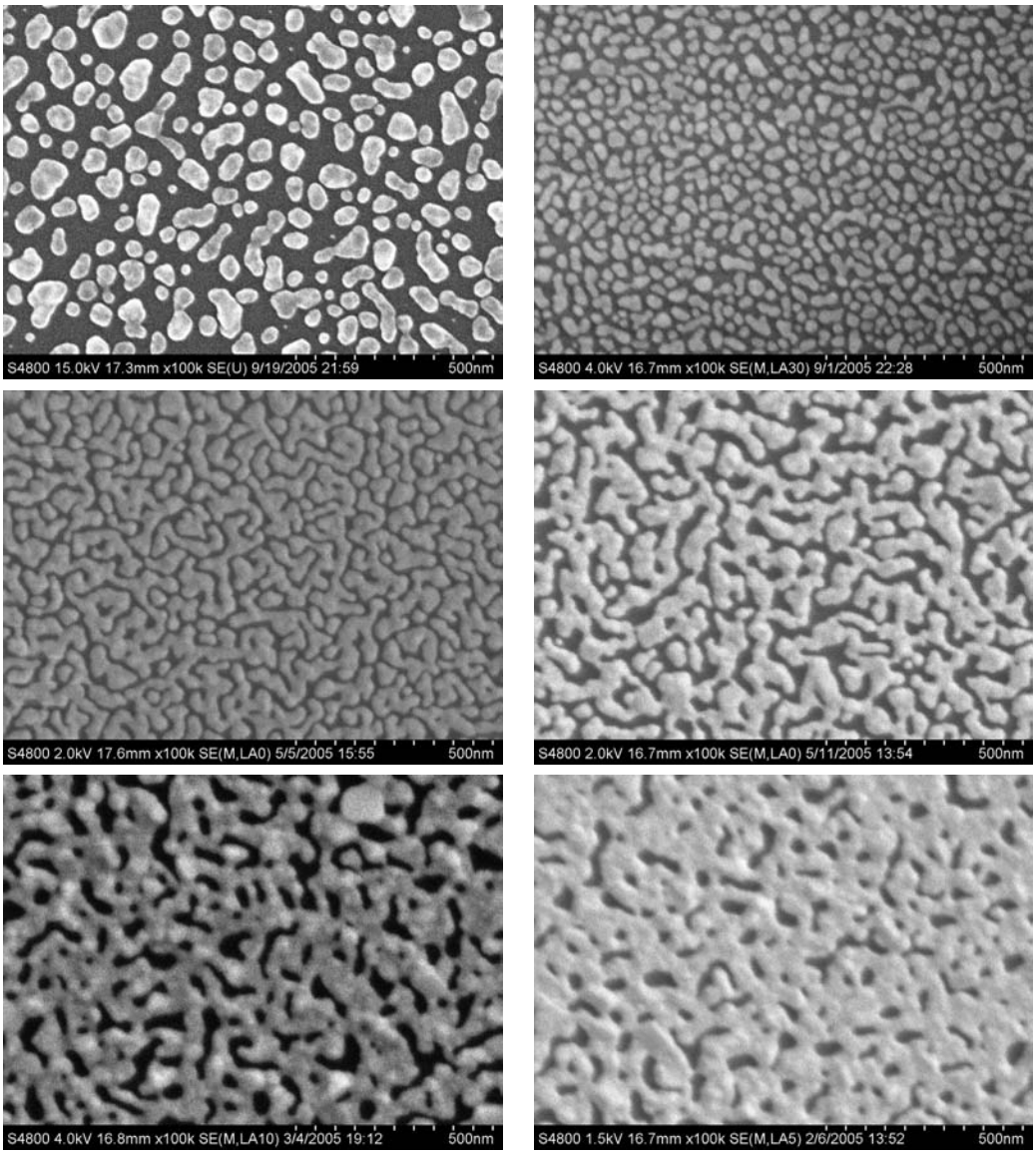

Figure 2.1. Semicontinuous silver films progress from disintegrated, isolated particles at low surface coverage (upper panels) through the percolation threshold (middle panels) and finally to a continuous film with dielectric voids and high metal coverage (lower panels). In these SEM images, the silver is white or light gray, while the dielectric substrate is dark gray or black.

formed in one of several electron-beam evaporator systems available in the Birck Nanotechnology Center cleanroom. All evaporation systems had an initial vacuum chamber pressure of 1×10^{-6} Torr (1 Torr = 133.3 Pa). The film thicknesses and deposition rates were monitored with a quartz crystal oscillator. Note that throughout this document, all fabricated layer thicknesses are given as mass average thicknesses measured with the quartz crystal deposition monitor.

The glass sections were covered first with a sublayer of silica (SiO_2, thickness 10-20 nm) followed by a silver layer (10-13 nm thickness) deposited at a rate of 0.05 nm s^{-1}. The fabricated substrates were stored in a desiccated or dry nitrogen environment and were typically used for applications within one month of fabrication. This ensured that the films did not undergo significant sulfidation or oxidation before use. Silver films in particular can rapidly sulfidize in an uncontrolled environment, causing degredation of the film properties.

Because of the very small amount of deposited silver material in our samples and the growth mode of silver, the silver layer is not continuous across the dielectric substrate. In fact, silver typically exhibits Volmer-Weber (island-like) growth on amorphous dielectrics like evaporated silica at low substrate temperatures [32]. Specifically, during the silver deposition process small isolated metal granules are formed first on the dielectric substrate. As the silver coverage is increased through additional metal deposition, the granules begin to coalesce together on the substrate surface, forming larger and connected islands. Still further metal deposition causes the film to reach the percolation threshold, which is the point at which the metal islands first produce a continuous path across the substrate. At the percolation threshold, the film changes character and becomes more metal-like than dielectric-like. Beyond percolation, still further metal deposition slowly fills in the spaces between the metal islands, and eventually a continuous, full metal film is formed on the substrate. In our samples, the deposition process is stopped before a continuous silver layer is formed, resulting in various sizes of silver particles and their aggregates.

Characterization and Analysis of Single-Layer Semicontinuous Films

Regardless of the fabrication process used to produce the film, there are several methods by which the success of a film fabrication process can be assessed. In this section we describe the techniques that we regularly employ to characterize various properties of our films and assess the fabrication results.

1. Ultraviolet/Visible/Near Infrared (UV/Vis/NIR) Spectroscopy

   Transmittance and reflectance measurements over a range of wavelengths can be used to determine information on the nanoscale structure of the semicontinuous films. The light impinging on a semicontinuous metal film will undergo transmission, reflection or absorption, with a very small portion (typically $< 5\%$) experiencing scattering. By measuring the intensity of light in each of these processes at different frequencies, one can judge whether the film structure supports resonant plasmon modes and where those modes exists in the spectral domain. In particular, using a spectrophotometer (Perkin Elmer model Lambda 950) with a 150-mm integrating sphere accessory, we measured the normally incident transmission (T,

%) and the 8° incidence reflection (R, %) of the samples over the 300 - 2500 nm wavelength range (UV to NIR). We then used this information to calculate the absorption (A, %) of the film using a simple formula

$$A = T_{glass} - R - T \tag{2.1}$$

T_{glass} is the bare glass substrate transmittance spectrum, which is typically above 92% for the visible and NIR wavelength ranges. Certain characteristics of this calculated absorption spectrum will indicate important features of the metal film. For instance, the presence and spectral positions of surface plasmon resonances are indicative of the structure of the film. In Figure 2.2, a representative absorption spectrum of a semicontinuous film near the percolation threshold shows an initial resonance near 550 nm and multiple resonances at longer wavelengths. This multitude of resonances overlap, causing a broad resonance wing to appear in the absorption spectrum. This broad-wavelength absorption is indicative of the fractal nature of the metal film morphology when the film is near the percolation threshold.

Plasmon excitation in a metal nanostructure results in strong light and particle interaction, and such excitation eventually leads to increased absorption relative to a thick metal film. In particular, we can compare the reflectance and absorption spectra of a film to obtain information on the film structure. At the frequencies where resonances occur, absorption increases. Typical UV/Vis/NIR absorption and reflectance spectra of a semicontinuous metal film are similar in shape and have a maximum at around 500 nm with a broad, flat wing into the longer wavelengths. The flat, broad absorption wing can extend into the mid-IR range and indicates that the nanostructure is resonant approximately equally at numerous wavelengths, which occurs for fractal film morphologies.

2. Infrared Spectroscopy

   We extended our spectral measurements beyond the UV/Vis/NIR range by using a Fourier-transform infrared (FTIR) spectrometer (Thermo-Nicolet) and special IR-transparent substrates to measure the infrared spectral response of our films at wavelengths out to 20 μm. This technique uses the Fourier transform of the time-domain coherence of a sample's response to obtain the frequency-domain spectrum of the sample [35]. In order to remove noise from the final spectrum, the system calculates the average Fourier transform of an ensemble of many time-domain measurements. For these measurements, the metal films were deposited on zinc selenide (ZnSe) substrates using the electron-beam deposition techniques described above. We used our FTIR results to ascertain whether a film is close to the percolation threshold or not, since the absorption of the film will show only a strong, flat and broad response for wavelengths in the mid-IR range when the metal nanostructure is at or very near the percolation threshold. Therefore, the silver film mid-IR absorption specrtrum allows us to sensitively determine how close the film is to the percolation threshold. In our recent publication, we also used FTIR measurements to observe the changes in the film response after infrared laser photomodification [36].

3. Scanning Electron Microscopy

   Scanning electron microscopy is an invaluable tool for visualizing and understanding the morphology of fabricated semicontinuous films. Several of these images appear throughout

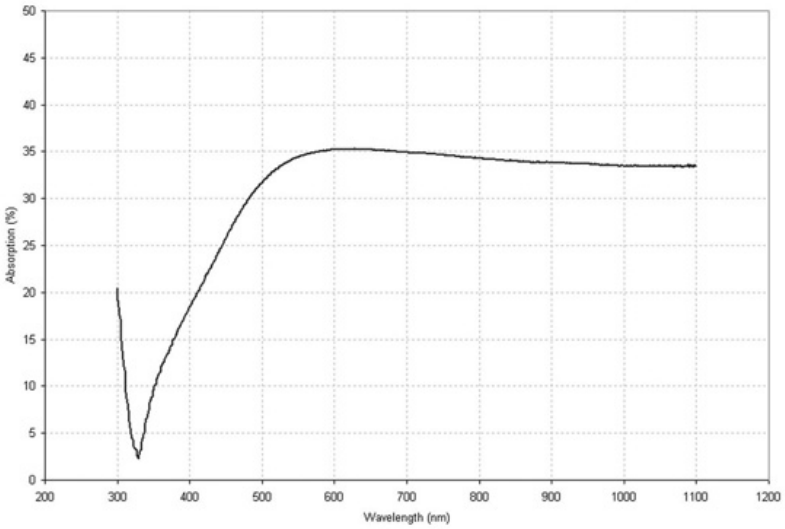

Figure 2.2. Representative absorption spectrum for a semicontinuous silver thin film near the percolation threshold fabricated by electron-beam evaporation. The flat, broad absorption wing into the near infrared range indicates that the nanostructure is resonant at a multitude of wavelengths approximately equally, which happens for fractal film morphologies.

this document, such as Fig. 2.4. We used a cold field-emission scanning electron microscope (FE SEM, Hitachi model S-4800) for our SEM studies. Digital images were obtained at several magnifications and across several locations on each sample, and aside from allowing us to visualize the film nanostructure, these images can also be processed using image-processing techniques to determine statistical information on the film, such as metal coverage ratio, fractal dimension, or others. The SEM images are also useful as a set of inputs to simulation calculations to retrieve the effective material parameters of the film. In this technique, the sample's spectral response can be calculated using the SEM images of the film. The simulation calculates the electric and magnetic fields in the structure under irradiation at various frequencies. Then the effective material properties ($\varepsilon_{eff}(\lambda)$ and $\mu_{eff}(\lambda)$) of the film can be found from the field distributions. The process is repeated for a number of SEM images, producing a set of results that can be averaged and compared to the measured spectral responses. This technique is described in more detail in Chapter 4.

4. Atomic Force Microscopy

Atomic force microscopy (AFM) has been used extensively for characterizing the surface topology of our samples. Atomic force microscopy utilizes a nanoscale probe to detect the Van der Wals forces near a surface and hence determine with great accuracy the height profile of the surface. Studies with AFM can tell us a great deal about a sample's surface roughness and physical height profile (if an appropriate step edge is available). We used an AFM system (Veeco Dimension 3100) in tapping mode with 10-nm silicon tips to measure our metal-dielectric film samples for surface roughness and physical film thicknesses. Scans were obtained at a variety of sizes, from 2 μm $\times$ 2 μm and larger, and at resolutions up to 512 data points per raster scan line. The root-mean-square (RMS, or simply the roughness) of the height profile was calculated from the AFM scans, giving us a measure of the smoothness of the film surface. A representative AFM image is shown in Figure 2.3, where the sample topology and caclulated sample roughness are presented.

Applications of Single-Layer Metal-Dielectric Films

The applications of semicontinuous, single-layer metal-dielectric films extend from optics to biology to communications and beyond. Some of the applications of plasmonics and photonics are discussed in the publications by Tuan Vo-Dinh and colleagues [37, 38, 39, 40, 1]. For our research, the applications of semicontinuous, single-layer silver films on dielectric substrates are discussed in Ref. [30, 41] and are also overviewed here. In this section we describe these applications in greater detail and discuss how the properties of the metal-dielectric film contribute significantly to the success of each application.

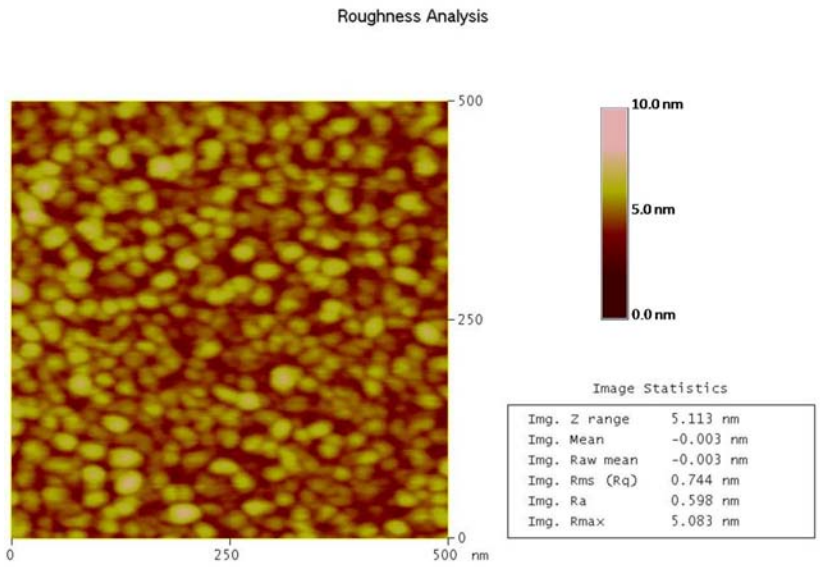

Figure 2.3. A representative AFM topology image and roughness measurement. The height of the sample surface is indicated by the color scale. The root-mean-square rougness and other sample statistics are listed in the AFM image.

Adaptive SERS-Active Substrates

Nanoscale plasmonic devices have been engineered for various purposes through the years. One purpose of note is surface-enhanced Raman scattering (SERS) spectroscopy, in which the inelastic scattering signal of a molecule is enhanced as much as a million times or more by the interaction of a plasmonic structure with incident light [42]. These SERS-active structures are often designed in such a way as to produce a predictable enhancement factor for only a narrow range of optical frequencies. In contrast to this, a nanoscale random metal-dielectric composite film with a statistically fractal morphology will support a broad band of resonance absorption frequencies. These semicontinuous films are relatively easy to fabricate, but difficult to optimize for a particular purpose. One of the significant challenges is to match the nanostructure morphology with a molecule of particular size and shape. In our research, we have contributed to the development of adaptive semicontinuous metal films which rearrange their nanoscale morphology in such a way as to match an analyte of interest. In our SERS-based biosensing research, we found that appropriately designed semicontinuous metal films will exhibit an adaptive behavior under deposition of molecular analytes in solution [31, 41]. The rearrangement tends to bring metal particles closer together, with analyte particles in the interstitial spaces between two or more metal particles. This final structure is particularly good for local electromagnetic field enhancement, and has been shown to produce excellent SERS results [43]. The adaptive feature of our samples is exciting because it allows the study of differently-sized analytes, from the very small organic molecules to larger proteins or viruses and beyond, using the same types of substrates [30].

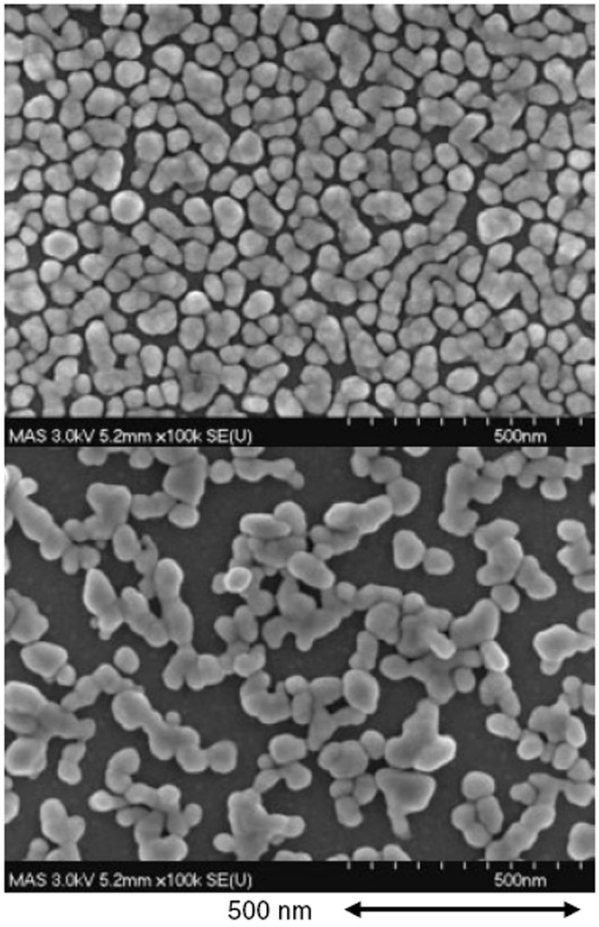

Figure 2.4. Adaptive silver film restructuring occurs during analyte solution deposition and drying, and this helps to create substrates particularly well-suited for SERS studies. The upper panel shows a scanning electron image of a semicontinuous silver film before protein solution deposition. The lower panel shows the same film after deposition of protein solution, restructuring and drying.

Adaptive metal films made with silver, herein called adaptive silver films (ASFs), have been successfully used in insulin isomer SERS studies, antibody-antigen binding experiments, protein phosphorylation studies and microarray experiments [44, 43, 30, 45, 46]. The interaction of biological molecules with a typical SERS substrate often leads to structural and functional changes in the molecules, and hence changes in the detected signal as compared to the normal (unenhanced) Raman signal. In our research on SERS substrates, we found that adaptive SERS-active substrates made from semicontinuous silver films coated on a silica sublayer do not lead to significant changes in the analyte. In fact, the biomaterial and the substrate act in concert to produce excellent Raman enhancement through local restructuring of the metal surface while at the same time preserving the properties (such as conformational state and binding activity) of the analyte [30].

The biomolecule-mediated restructuring illustrated by FESEM images in Fig. 2.4 results in aggregates of closely spaced particles covered with biomolecules. This is in contrast to the rather disintegrated particles of the initial film before analyte deposition. Depending on the mass thickness of the initial film, small or large fractal-like aggregates can be formed. The analyte SERS signal, normalized to unit metal mass coverage, is comparable for both the small and large metal particle aggregates that we examined, and SERS enhancement is high enough to detect as little as a monolayer of analyte [30].

In other biomolecule studies with ASFs, we examined the SERS signal from insulin isomers, which are difficult to distinguish by any methods other than expensive, time-consuming chemical analyses. Using our ASF substrates, however, we were able to distinguish between two isomers of insulin [43]. This result confirmed that the conformational state of the analyte in our ASF studies is maintained, since the isulin isomers differ in their conformational states. The measured macroscopic enhancement factor for insulin on our ASF substrates relative to the normal Raman signal of insulin on quartz was about 3×10^6, which is among the largest observed in the literature for random metal-dielectric films [30]. It is important to note that, in general, non-adaptive films that do not show restructuring are created by optimizing either evaporation parameters (sublayer, deposition rate, mass thickness, etc.) or the contents of the biomolecule solution. This means that non-adaptive substrates should be tailored to specific biomolecule solutions, or vice versa. Clearly, such changes can affect metal structures or biomolecule adsorption, which makes it impossible to compare SERS results on adaptive films directly with those from nonadaptive films. Regardless, from analysis of FESEM images and SERS enhancement results, the observation is that there is no detectable SERS without restructuring.

Nanostructured ASFs demonstrate significant advantages over static SERS-active substrates. The characterization of these films leads to the conclusion that ASFs experience fine restructuring under biomolecule deposition, such that conformation and functionality are preserved. In addition, the biomolecule-mediated restructuring produces excellent conditions for SERS enhancement. The interaction of the silver film with the biomolecule solution even acts to stabilize the system, making it resistant to wash processes [30]. Our examples of ASFs in SERS studies show that ASFs preserve the secondary structure of insulin and have a high SERS sensitivity in detecting conformational distinctions of nearly identical insulin isomers. In addition, we have found that SERS substrates based on ASFs can be used for direct, label-free detection of protein binding at a monolayer level (data not shown here, see [45] for more information). Our ASF substrates even allow

independent validation of antibody-antigen binding by conventional chemiluminescence and fluorescence methods [30], which means that multiple measurement techniques can use the same substrate. Clearly, ASFs show great promise for detection and analysis of biomolecules, even at very low surface densities.

Infrared Obscurants and Filters

Some of the research performed by the Shalaev group during the term of this Sandia-sponsored fellowship has focused on tailoring semicontinuous metal films for use as mid-IR plasmonic filters [36]. As mentioned previously, semicontinuous films with appropriate fractal-like morphologies will absorb frequencies into the mid-IR range (out to 20 μm or more). The first step in creating filters or obscurants is to fabricate samples with significant absorption in the mid-IR range, which was aided by our previous experience in fabricating semicontinuous metal-dielectric films with predetermined properties. Subsequent photomodification procedures changed the initial samples by selectively destroying the metal clusters or structures resonating at and above the incident photomodification wavelength. As with many of our samples, we studied the metal nanostructure and optical properties of the these samples using UV/Vis/NIR and FTIR spectroscopy and SEM imaging. We found that film extinction spectra can be tailored by carefully adjusting the deposition conditions during sample fabrication. We also found that post-fabrication photomodification with both nanosecond and picosecond laser pulses in the mid-IR range can provide a spectrally selective tool for further control of a film's optical response.

In these studies, silver films of various thicknesses (from 6.8 to 11 nm) were deposited on planar, polycrystalline zinc selenide (ZnSe) substrates at room temperature using techniques and procedures similar to those mentioned in Section 2. The ZnSe windows (Laser Research Optics, 25 mm diameter, 2 mm thickness) were used as substrates due to the material's transparency in the mid-IR. In some of these samples, we did not use a silica sublayer, and hence we found it necessary to experimentally determine the percolation threshold of a silver island film on polycrystalline ZnSe in order to optimize the silver film extinction in the mid-IR range. For those samples that were precoated with silica, we found the percolation threshold to be similar to that of silver films deposited on glass substrates.

Under our evaporation conditions, a 6.8-nm Ag film evaporated directly on ZnSe showed a densely packed metal structure above the percolation threshold, with a coverage ratio of about 0.7 and high extinction (due to high reflection). Since the main goal of this work was to study the photomodification effects on the structural and optical properties of SMFs, we decided to increase the mass thickness percolation threshold of our films in order to increase the extinction level of the evaporated Ag films at percolation. We therefore decided to evaporate an intermediate layer of silicon dioxide on the ZnSe substrates, since it is known that Ag films grown on silica layers with glass substrates exhibit a percolation threshold mass thickness above 11 nm [30]. Hence, for some samples, a 10-nm silica sublayer was evaporated on the ZnSe substrate at deposition rate of 0.1 nm s^{-1} prior to the Ag evaporation. As a result of the addition of this layer, the percolation threshold mass thickness of the Ag films increased from less than 6.8 nm to about 10.5 nm. For all of these studies, the film extinction was measured (extinction = reflectance + absorption). This is because

the reflectance measurements in the FTIR system are difficult and time-consuming to perform, and extinction itself provides the necessary spectral information on changes in the sample arising from photomodification.

The samples were irradiated with pulsed laser light at 10.6 μm using one of two laser systems. The first laser is a pulsed MTL-3GT Mini TEA CO2 Laser (Edinburgh Instruments Ltd.) operating at 10.6 μm. The laser radiation was linearly polarized, and the pulse duration was 50 ns. The second laser is a nonlinear difference-frequency generator (NDFG, Light Conversion) pumped by a laser system containing an optical parametric amplifier (TOPAS, Quantronics/Light Conversion) and a Ti:sapphire regenerative amplifier (Spitfire, Spectra Physics). The NDFG is pumped by an optical parametric oscillator and is capable of generating 2-ps pulses in the 3 - 20 μm range with a repetition rate of 1 kHz. For the photomodification experiments with this laser, the beam was focused with a ZnSe lens to a spot diameter less than 200 μm in order to obtain an energy density sufficient for the photomodification process.

The samples were exposed to a varying number of laser pulses to observe the effect of the pulse number on the spectral changes in the films. Our results show both polarization- and wavelength-selective changes in the extinction spectra of the films as well as changes in the film metal nanostructure [36]. Both of the photomodification methods show similar spectral changes in the final extinction spectra, and both also result in spectral features for the samples that are characteristic of long-pass filters (see Fig. 2.5).

The photomodification energy density threshold (that is, the energy density at which photomodification begins to occur) for our semicontinuous metal films in the case of 50-ns pulses is approximately 200 mJ cm^{-2}. This threshold is about 10 - 20 times higher than that reported for similar structures in the visible and near-IR ranges [36]. In the case of photomodification with picosecond pulses, the energy density needed for detectable changes is below 10 mJ cm^{-2} and is similar to the results reported for the visible and near-IR ranges for fractal silver nanostructures [36]. However, the number of pulses needed in our case is orders of magnitude higher.

The observed changes in the silver nanostructure of the films are a result of a local temperature increase in specific areas of the metal structure. Electron microscopy images show that the areas of changes are localized, indicating very non-uniform absorption and temperature distributions. The difference between the restructuring occurring for nanosecond and picosecond pulses comes from the higher energy localization for the shorter pulses. For the case of nanosecond pulses, the energy absorbed in the vicinity of a hotspot is partially transferred to other areas of the metal structure due to the relatively long pulse duration. For the picosecond pulses, however, the changes in the nanostructure occur before the absorbed energy can spread to neighboring metal structures. As a result, the total volume of heated metal is much lower for the case of picosecond pulses. This results in lower photomodification energy density threshold and more localized structure changes.

In both nanosecond and picosecond photomodification methods, the results show a decrease in measured extinction for wavelengths beyond the incident laser wavelength. This technique allows the creation of long-pass filters for the mid-IR range, in agreement with earlier theoretical work performed in the Shalaev group [47].

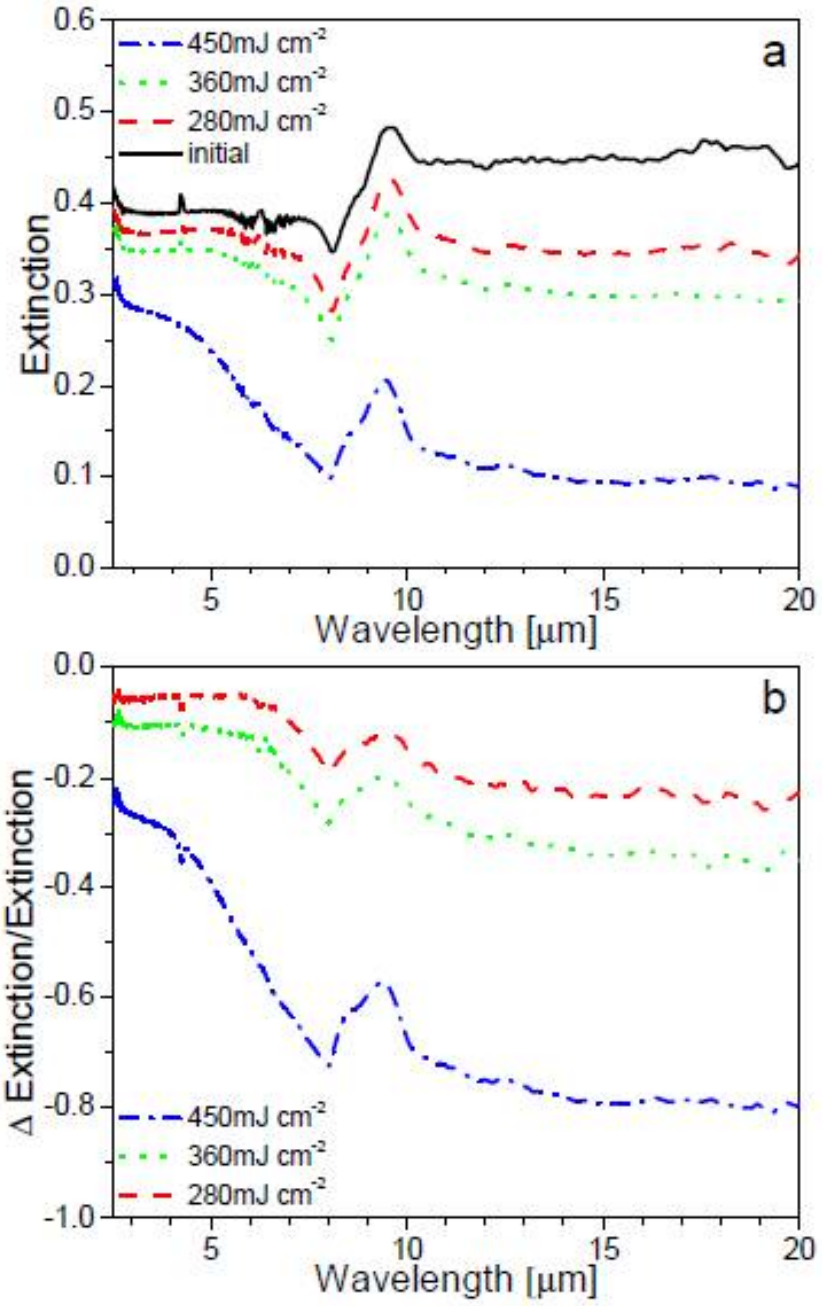

Figure 2.5. Spectral changes in a semicontinuous silver film after photomodfication with nanosecond pulses from a 10.6 μm CO_2 laser. (a) Sample extinction spectra after photomofication at various incident energy densities, and (b) sample extinctions normalized to the unmodified sample. The photomodification results in changes to the nanostructure of silver island films, causing selective transmission of wavelengths beyond the photomodification wavelength. From [36]

Chapter 3

Multilayer MDC Films

This chapter reviews the research work that has been accomplished in the area of multilayer semincontinuous films, which are called metal-dielectric composite (MDC) films here to distinguish them from single-layer samples. There are two broad and partially overlapping types of such films: samples with distinct layers and samples with indistinct layers. We consider each type in turn, presenting in detail the research results on each of the two types of MDC structures studied in our work.

Multilayer MDC Films with Distinct Layers

In addition to single-layer semicontinuous films, multilayer samples have been studied in our work. This section considers multilayer films that have distinct layers, such that in cross-section views one can distinguish between a metal layer and it's adjacent dielectric layers. As an example, Figure 3.1 shows the transmission electron microscopy cross-section views of several Au-SiO_2 with different layer thicknesses [48] (see also Refs [49, 50] for similar work with Ag-Si_3N_4 multilayers). In some images, the layers are clearly distinguishable. In others, however, it is really not possible to say where one layer ends and another begins; these types of films will be discussed in the next section. In reality, the fabrication parameters and chosen materials determine whether a multilayer film will show distinct or indistinct layers. For thicker individual films (well beyond a single monolayer), the multilayer structure will show distinct layers. For thinner films, the details of the growth processes for each constituent play a strong role in the film structure [32, 48]. We typically use silver and a transparent dielectric material like silica (SiO_2) or alumina (Al_2O_3) in our samples. These systems (Ag on silica or Ag on alumina) exhibit Volmer-Weber growth for low metal thicknesses [32, 48], and hence for thin metal layers but thick dielectric layers, the layer structure is still distinct. With thin metal layers and thin dielectric layers, however, the structure is indistinct and a true composite mixture is observed.

Metal-dielectric multilayer systems with distinct layers have been used in research on superlensing and UV bandpass filters, among others [51, 52]. Notably, the use of multilayer metal-dielectric film with relatively thick (10s of nm) films can show a blue shift of the bulk plasmon resonance frequency, providing transparency at UV frequencies that would normally be absorbed through exitation of interband electron transitions in the metal [52, 12].

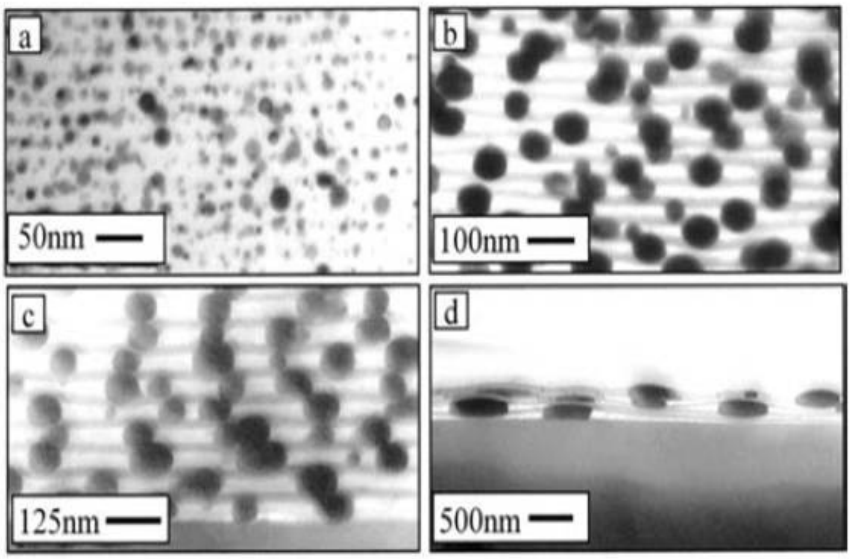

Figure 3.1. Transmission electron microscope (TEM) cross-section images of gold and silica multilayer films after annealing. The images show distinct layers for some samples, and indistinct layers for others. Gold film thicknesses are (a) 1 nm, (b) 4 nm, (c) 8 nm, and (d) 16 nm. The shapes of the metallic inclusions range from approximately spherical in (a) to nonspherical in (d). From [48]

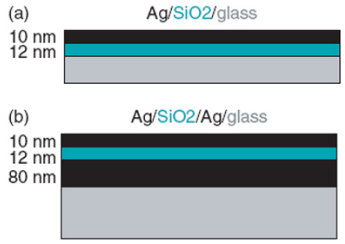

Figure 3.2. A schematic showing (a) the stackup of a typical single-metal-layer semicontinuous metal film, and (b) a multilayer sandwich film structure consisting of an additional bulk metal layer below a dielectric spacer.

Our experiments with multilayer samples consisted of a bulk metal layer below our usual semi-continuous film structure (see Fig. 3.2). Our work revealed a promising way to further improve these films for applications such as SERS or other surface-enhanced processes. Our group's previous work showed that a nanostructured metal film positioned near a mirror-like metal surface with an intermediate dielectric layer can show dramatic changes in the film's optical properties as compared to a similar single-layer film [30]. The preliminary results on such samples indicated that they provide improved enhancement and applicability for various projects [30].

In our initial studies, we fabricated sandwich structures (see Figure 3.2) containing a bulk silver layer (80 nm) deposited on glass, followed by a layer of SiO_2 (10 nm) and finally a 12-nm nanostructured silver film. These samples were used in SERS studies in order to compare the results with similar nanostructured films lacking the bulk metal layer. Therefore, relative to the single-layer structure, the sandwich sample includes only an additional sublayer of bulk silver. The bulk silver layer provides an additional enhancement of the local fields caused by the interaction between the fields around the metal nanostructures and their images in the bulk layer, and by far-field interactions between the metal particles [45]. We performed test experiments with these multi-layer structures using three analytes: human insulin, anti-human interleukin 10 and anti-human interleukin 10 incubated with 1 nM R6G (a Raman-active dye molecule). In particular, in our experiments with insulin we observed 28-38 counts s^{-1} mW^{-1} from the sandwich structure (vs 1.5-4 counts s^{-1} mW^{-1} for the substrate used for comparison and 7 counts s^{-1} mW^{-1} for maximum signal over all non-sandwich samples). From our data, we conclude that the multi-layer sandwich structure provides a signal increment of at least 4-5 [45].

In order to extend these studies, we fabricated a set of samples to investigate the effect of the dielectric spacer layer thickness on the properties of the overall sample. In these studies, we fabricated five samples with different intermediate silica layers between the bulk silver layer and the thin silver layer. In order to accomplish this, five substrates were precoated with 80 nm of silver in a single evaporation cycle. Then, five separate evaporations were performed to coat each sample with a different thickness of silica. Finally, all five samples were concurrently coated with a 12-nm silver film. All these evaporations were done on the same e-beam evaporation system and were

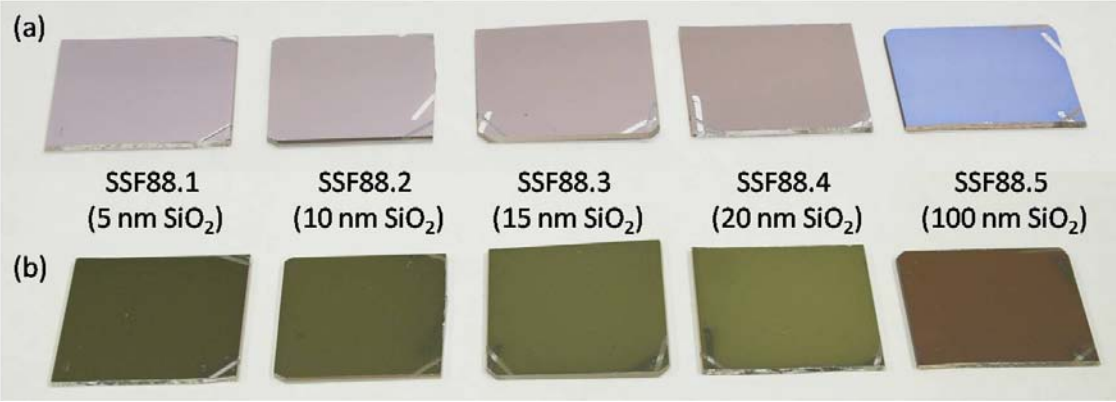

Figure 3.3. Multilayer sandwich samples (SSF88) were fabricated with varying dielectric spacer layers. The samples show varying coupling strengths, resulting in different colors in the reflected light. (a) Samples photographed without a flash (ambient light only), and (b) with a camera-mounted flash.

completed consecutively in an effort to minimize variations between samples. The samples, named SSF88.1 through SSF88.5, are shown in Figure 3.3, where the optical images clearly show differences in color in each sample. These color changes arise because of different coupling strengths between the upper and lower silver layers in each sample. Reflectance spectra for SSF88.1 (5 nm silica spacer) through SSF88.5 (100 nm silica spacer) are shown in Figure 3.4 and indicate that the reflectance changes appreciably as the dielectric spacer thickness varies. In particular, SSF88.5 (with a 100-nm silica layer) exhibits a very different response than the samples with thinner layers. This is the result of reduced coupling between the bulk silver underlayer and the nanostructured silver film on top for SSF88.5. This is also seen in the photographs of the films (Fig. 3.3), where the color of SSF88.5 is quite different than those of the other four samples. It is the coupling strength (and hence, the dielectric spacer thickness) that determines the additional contribution to local field enhancement from the bulk silver sublayer. Studies like this one have helped us determine the optimal dielectric spacer thickness to be on the order of 10-20 nm. However, note that these studies are at least partially suspect because there are hidden variables in our results. In particular, the fact that seven separate evaporations were required to produce the SSF88 sample set casts a shadow over our results, since fabrication variables such as chamber pressure and contamination of waiting samples are not controlled in this study. The solution to this issue is discussed in Ref. [53], but we do not have the space for it here. Briefly, we upgraded existing fabrication equipment in order to create samples with complex cross sections, or even to make two samples with different layers in a single pumpdown cycle. This gives us the ability to directly compare results from multilayer films with different layer thicknesses.

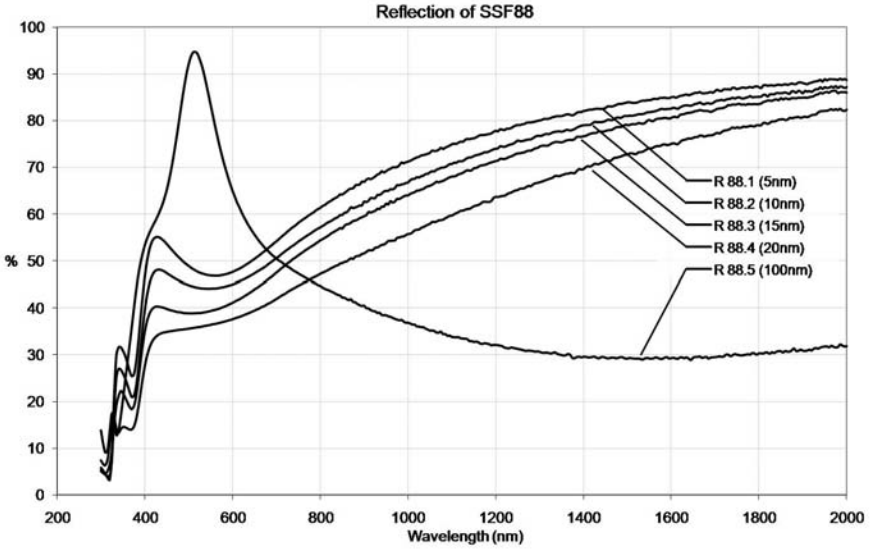

Figure 3.4. Reflectance spectra for SSF88.1 (5 nm spacer) through SSF88.5 (100 nm spacer) show the variation of the sample responses as the silica spacer thickness is changed. Notably, the sample with very thick spacer (100 nm, SSF88.5) shows a very different reflectance response than the other, thinner spacer samples.

Multilayer MDC Films with Indistinct Layers

For layers deposited well beyond a few monolayers in thickness, an alternating multilayer structure will exhibit distinct layers that are easily distinguishable. However, the case of thinner (less than a few monolayers) metal-dielectric films is more complex. For these multilayer films, the details of the growth processes for each constituent play a strong role in the final film structure [32, 54]. We typically use silver or gold and a transparent dielectric material like silica (SiO_2) or alumina (Al_2O_3) in our plasmonic multilayer samples. The metal-on-oxide growth systems (Ag on silica or Ag on alumina) typically exhibit Volmer-Weber growth for low metal thicknesses [32, 50, 55], while the oxide-on-metal growth is often completely wetted (the dielectric coats the surface uniformly) [32]. Hence for thin metal layers but thick dielectric layers, the layer structure is still distinct. With thin metal layers and thin dielectric layers, however, the structure is indistinct and a true 3D composite mixture is observed. Such composites can be used, for example, as tunable near-field superlens (NFSL) devices [56], which has been our focus in studying metal-dielectric composite (MDC) multilayer films.

Near-Field Superlenses from Multilayer Metal-Dielectric Composites

One very interesting application of MDC films is a device known as a near-field superlens. This structure acts to transfer both propagating and evanescent fields from one side of the lens to the other, allowing for sub-diffraction resolution. Planar slab near-field superlenses made of bulk silver, for example, also show this effect. However, the silver slab superlens, although realizable (see, for example, Refs. [57, 58]), suffers in that it only operates as a superlens for a single frequency. MDC-based near-field superlenses, however, would be tunable by varying the filling factor of the metal-dielectric composite, making these structures more attractive for applications than bulk metal near-field superlenses. Such tunable near-field superlenses were considered by Wenshan Cai, a groupmate in Prof. Shalaev's group at Purdue [56]. An extension of Wenshan's analysis was perfomed by Shi *et al.* shortly thereafter and included nonspherical inclusions in the analysis [59]. Since tunable near-field superlenses are an important aspect of our research, here we describe some of the work and analyses previously accomplished in this area by Cai *et al.* and Shi *et al* to provide a thorough introduction to the concepts.

A planar material slab with simultaneously negative permittivity and permeability can focus propagating waves and enhance evanescent waves, thereby acting as a perfect lens or superlens that does not suffer from the diffraction limit [60]. The operation of a perfect lens requires that $\varepsilon_1 = -\varepsilon_2$ and $\mu_1 = -\mu_2$, where ε_1 and μ_1 are the permittivity and permeability of the perfect lens and ε_2 and μ_2 are those of the adjacent host material. If the source object is close to the slab, however, the electrostatic approximation is valid and the superlensing requirement can be relaxed to $\varepsilon_1 = -\varepsilon_2$ [60]. This condition can be readily satisfied by metals such as gold and silver at particular frequencies, creating a practical NFSL. If a resonant nanoantenna is placed close to the NFSL, the lens can generate the image of the antenna's hot spot on the other side of the lens. Unfortunately, NFSL designs based on bulk metal can operate only at a single frequency, determined by the material properties of the bulk metal and host. For the best plasmonic material, silver, and with common

photoresists as the host, this operational frequency turns out to be in the near ultraviolet [57]. In contrast, the operational frequency for a metal-dielectric composite superlens can be varied through the visible and near-infrared ranges by adjusting the metal filling factor [56]. Therefore, rather than limiting our analysis to bulk metal lenses, we consider the conditions for NFSL operation using a metal-dielectric composite.

We mentioned previously that electromagnetic field enhancement from plasmonic structures can be used in a variety of applications, including SERS [44], SERIRA [36, 61], and fluorescence. This is due to the fact that certain plasmonic structures, such as fractal metal films [62] or nanoantenna arrays [63] can support a highly efficient, localized surface plasmon resonances and produce a significantly enhanced and highly confined electromagnetic field known as a 'hot spot' [20]. However, published literature suggests that the fluorescence and SERS enhancement depend on the separation between the fluorophores and the metal nanoparticles, and if the fluorophores are too close to the nanoparticles, the fluorescence may be quenched instead of enhanced (see [63] and references therein). Another problem is that when in direct contact with metal surfaces, some molecules experience significant structural (denaturation) and/or functional changes (see [45] and references therein). A metal-dielectric near-field superlens (NFSL), offers a possible solution to these problems. The composite lens provides the ability to image the high local fields produced by a SERS-active or fluorescence substrate to the other side of the composite lens, where bio-molecules or other analytes can be placed. The computational study of such a system, undertaken recently by our group [63], included the simulation of an optical nanoantenna system placed near a composite superlens, with an emphasis on determining how well the superlens translates the enhanced field produced by a nanoantenna pair to the far side of the lens. Our EMT and finite-element method (FEM) simulations showed that a nanoantenna-superlens device can indeed produce a translated hot spot or enhanced field region on the image side of a near-field superlens, albeit with a somewhat decreased amplitude. This simulation confirmation is an important step in composite NFSL research because it provides a comparison for fabricated samples and helps to direct future experimental work. These results are discussed in detail in Section 4.

The optical properties of metal-dielectric composites can be described by Bruggeman's EMT formalism [64, 65, 66]. The dependence of the effective dielectric permittivity ε on the light wavelength λ and on the metal filling factor p is the key to realizing the tunable NFSL. The operational wavelength defined by the condition $Re(\varepsilon_e(\lambda_{op})) = -\varepsilon_h(\lambda_{op})$ depends on p and thus can be controlled by varying the metal filling factor. This makes it possible to tune the operating point over a wide wavelength range of interest.

Figure 3.5, from the analytical results of Cai *et al.* [56], shows the required metal filling factor p for superlens operation using an Ag-SiO_2 composite lens. For each kind of host material, the lower limit of the operational wavelength range corresponds to the pure metal $p = 1$ case. A lower metal filling factor is required for a longer operational wavelength. For very long wavelengths, the required filling factor for the composite approaches the percolation threshold where the broad resonance peak in ε_e reduces the super resolution effect. In Fig. 3.5 the upper limit of the possible wavelength range is determined so that $Im(\varepsilon_e)/Re(\varepsilon_h) = 0.1$ at the longer wavelength end of the operational range. As seen in Fig. 3.5(a), with an Ag-SiO_2 composite as the lens material, the operation ranges are 0.47 to 0.67 μm for SiC host material and 0.61 to 1.10 μm for Si host

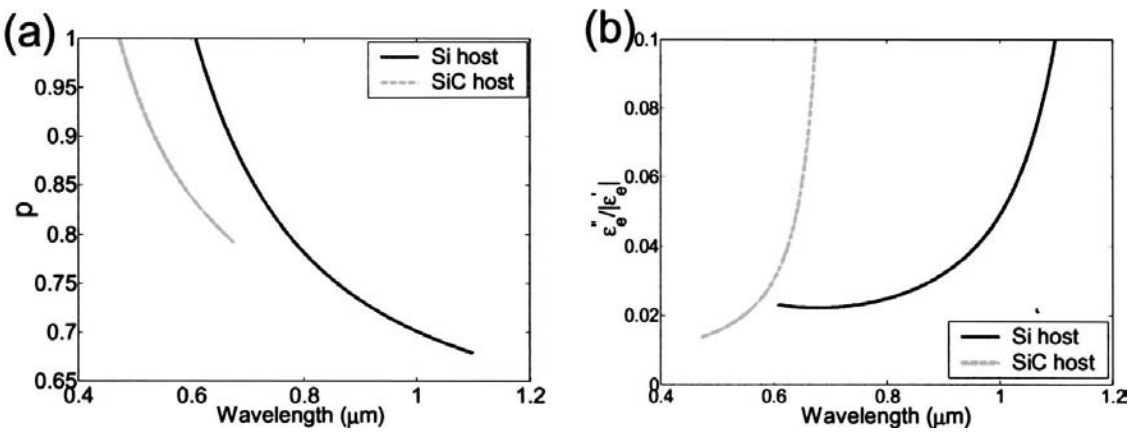

Figure 3.5. Performance of an Ag-SiO_2 composite lens with Si or SiC as the host medium. (a) The required metal filling factor p for different wavelengths. (b) The value of $Im(\varepsilon_e)/Re(\varepsilon_h)$ for different wavelengths (From [56]).

material. Therefore, combining the results of the two host media we can achieve a possible operational wavelength range of 0.47 to 1.10 μm, which covers nearly the whole visible spectrum and the shorter part of the NIR band. The operational range can be expanded even further by using other host media or other constituent materials for the metal-dielectric composite. The value of $Im(\varepsilon_e)/Re(\varepsilon_h)$, which is related to the loss in the lens structure, is plotted as a function of the operational wavelength in Fig. 3.5(b).

Composite NFSL Prototype Samples

We have designed, fabricated and studied a variety of samples as prototype systems for use in NFSL designs. By tailoring the metal volume ratio, we are able to produce samples that exhibit properties suitable for NFSL functionality. The results of fabrication and characterization of several sets of composite films for prototype superlens designs are shown here. All films were fabricated in a process similar to those mentioned previously in this document. Silver and silica layers were evaporation at rates of 0.05 nm s^{-1} and about 0.1 nm s^{-1}, respectively. The explicit stackup of each multilayer film is given in Table 3.1. The films have been fabricated in an attempt to study the parameter space of composite NFSL prototype films, including parameters such as the overall film thickness, the metal volume (filling) fraction, and the number of pairs of metal/dielectric layers. How these parameters vary for each film is given explicitly in Table 3.2 (Number of Layers), Table 3.3 (Total Thickness) and Table 3.4 (Metal Ratio). As an example, Table 3.2 shows three samples that vary only in the number of metal layers, while total thickness and metal volume ratio are kept constant. Note that when calculating total film thickness, the first layer of silica was not considered as it does not affect the effective medium theory calculations since the initial substrate is glass. The film set named SSF155 was used as the initial reference for all parameters in order to

minimize the number of evaporations required to complete the study.

All samples were characterized using FESEM, AFM and UV/Vis/NIR spectrometry. Representative FESEM images of the films are shown in Figure 3.8, where each film is shown at the same magnification. It is clear from the images that the nanostructure of the films is different for different parameters of interest. For example, very thin metal layers ($\sim$ 3 nm) produce isolated particles that have very small ($\sim$ 10 nm) in-plane sizes (see SSF157 and SSF160). Thicker metal layers ($\sim$ 6-8 nm) produce isolated but slightly larger particles (see SSF155 and SSF162). Still thicker layers ($\sim$ 12 nm) produce long islands of metal, often connected over substantial distances (see SSF158 and SSF159). This is expected, since 12 nm is approximately the percolation threshold for silver grown on silica. The images show that the various films, though they would be treated the same in EMT calculations), clearly have very different silver island particle sizes and shapes, leading to different spectral responses. The edge profile of one sample (SSF162) is shown in Figure 3.9, where the film was deposited onto a silicon(100) wafer concurrently with the glass substrates. The Si wafer was then cleaved and the edge imaged by FESEM in order to observe the structure of the film in cross section. From the image we can see that the film exhibits a structure similar to that seen in top-view FESEM images throughout the film depth. Other side view images strongly support the results of AFM measurements, including physical height and roughness values (not shown).

All AFM scans were collected on a Veeco Dimension 3100 atomic force microscope system using 10-nm Si tips in tapping mode. The samples were scratched with sharp tweezers in order to characterize the film physical thicknesses. Height profiles from central locations in the samples were also collected and analyzed for roughness using 5×5 μm and 2×2 μm scans, both collected at 1 Hz with 512 samples per raster line. The resulting images were processed in two AFM image analysis programs (NanoScope from Veeco and WSxM [67]), with similar results from both programs. Step heights and root-mean-square (RMS) roughness values are given for the samples in Table 3.5. In Table 3.5, the "AFM-XTAL" column shows the difference between the measured step height of the film (AFM) and the total thickness reported during fabrication by the quartz crystal monitor (XTAL). This difference varies for each film, which could indicate variations in the fabrication processes for each sample. Also, the RMS roughness values in the table are the average values from the NanoScope and the WSxM program results. Finally, the ratio of metal to dielectric thickness in the top two layers (labeled TLR) is given in the table, as this value seems to have some effect on the final film roughness. This may be due to the way the silica layer forms on silver island films. Our results show that the silica appears to fill in the gaps between silver particles, causing a lower final surface roughness than without the silica. Hence, thicker silica layers tend to smooth out the roughness more than thin layers; this is the trend seen in the Table 3.5 data.

The transmittance, reflectance, and absorption (T/R/A) spectra of the films are presented in individual figures at the end of this section. As with our single-layer films, each sample in this set was measured with normally incident light (for T) and 8° incidence (for R) in the UV/Vis/NIR range (350 - 2500 nm). Absorption was calculated as before from the transmittance and reflectance measurements, and diffuse scattering was assumed negligible. Sscattering measurements for one film (SSF155) confirm that diffuse scattering is indeed below 5% for all wavelengths of interest.

Table 3.1. Approximate stackup for various composite films used as prototype samples for near-field superlens designs (all values in nm).

SSF155	SSF157	SSF158	SSF159	SSF160	SSF161	SSF162
	1.6 SiO_2					
	3 Ag					
	1.6 SiO_2					
	3 Ag					
	1.6 SiO_2					
	3 Ag					
	1.6 SiO_2					
	3 Ag					
5.0 SiO_2	1.6 SiO_2		5.5 SiO_2	1.6 SiO_2	6.3 SiO_2	1.3 SiO_2
6 Ag	3 Ag		10 Ag	3 Ag	3 Ag	8 Ag
2.7 SiO_2	1.6 SiO_2		5.5 SiO_2	1.6 SiO_2	6.3 SiO_2	1.3 SiO_2
6 Ag	3 Ag		10 Ag	3 Ag	3 Ag	8 Ag
2.7 SiO_2	1.6 SiO_2	6.6 SiO_2	5.5 SiO_2	1.6 SiO_2	6.3 SiO_2	1.3 SiO_2
6 Ag	3 Ag	12 Ag	10 Ag	3 Ag	3 Ag	8 Ag
2.7 SiO_2	1.6 SiO_2	6.6 SiO_2	5.5 SiO_2	1.6 SiO_2	6.3 SiO_2	1.3 SiO_2
6 Ag	3 Ag	12 Ag	10 Ag	3 Ag	3 Ag	8 Ag
7.7 SiO_2	10 SiO_2	10 SiO_2	10 SiO_2	10 SiO_2	10 SiO_2	10 SiO_2
Glass Substrate	Glass Substrate	Glass Substrate	Glass Substrate	Glass Substrate	Glass Substrate	Glass Substrate

Table 3.2. Composite films with varying layers.

Set Name	Total Thickness (nm)	Paired M/D Layers	Metal Ratio
SSF155	37.1	4	0.65
SSF157	37.1	8	0.65
SSF158	37.1	2	0.65

Table 3.3. Composite films with varying thicknesses.

Set Name	Total Thickness (nm)	Paired M/D Layers	Metal Ratio
SSF155	37.1	4	0.65
SSF160	18.6	4	0.65
SSF159	61.8	4	0.65

Table 3.4. Composite films with varying metal ratios.

Set Name	Total Thickness (nm)	Paired M/D Layers	Metal Ratio
SSF155	37.1	4	0.65
SSF161	37.1	4	0.32
SSF162	37.1	4	0.86

Table 3.5. Measured heights and roughness values for various multilayer metal-dielectric samples intended as prototype NFSL films. See Figure 3.6 for definitions of quantities listed in the table.

	T (XTAL)	T (AFM)	AFM-XTAL	TLR (SiO_2/Ag)	RMS $2\mu m \times 2\mu m$	RMS $5\mu m \times 5\mu m$
	nm	nm	nm		nm	nm
SSF155	47.1	52.1	5.0	0.833	1.69	1.76
SSF157	47.1	55.8	8.7	0.533	1.87	2.02
SSF158	47.1	47.2	0.1	0.55	1.64	1.83
SSF159	71.83	76.3	4.47	0.55	1.41	1.5
SSF160	28.55	22.6	-5.95	0.533	1.82	2.09
SSF161	47.1	48.1	1.0	2.1	0.67	0.7
SSF162	47.1	55.1	8.0	0.163	2.4	2.51

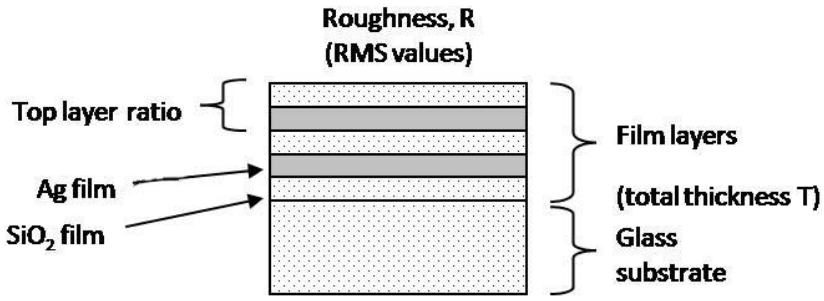

Figure 3.6. Explanation of dimensions used in Table 3.1.

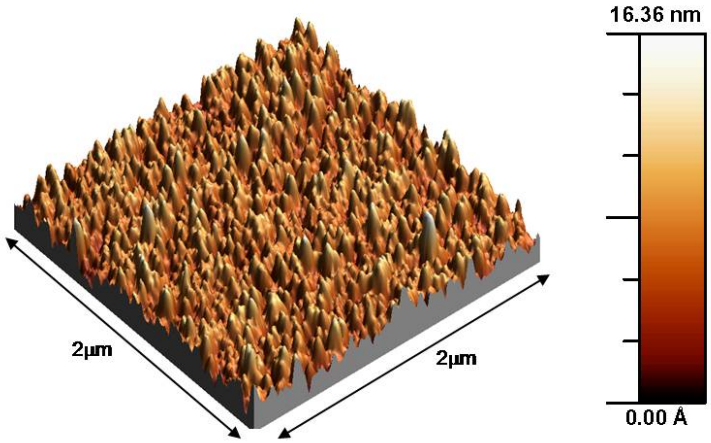

Figure 3.7. A 2 μm x 2 μm AFM scan of the top surface of SSF157. The height data has been processed to show a 3D rendering, and the color scale for height is shown at the right.

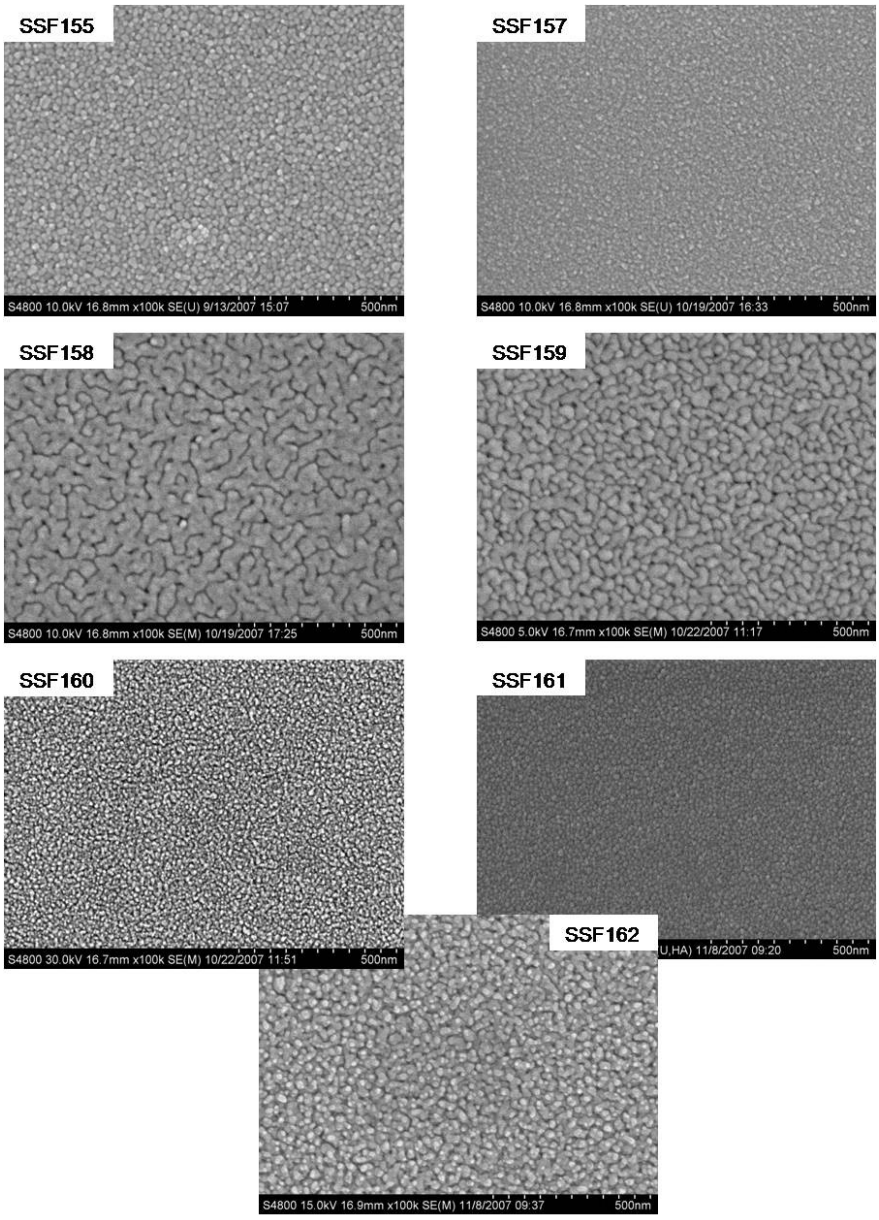

Figure 3.8. FESEM images of several composite metal-dielectric films fabricated as NFSL prototypes. The images show that the films, though treated the same in EMT calculations, clearly show different island particle sizes and shapes, leading to different spectral responses.

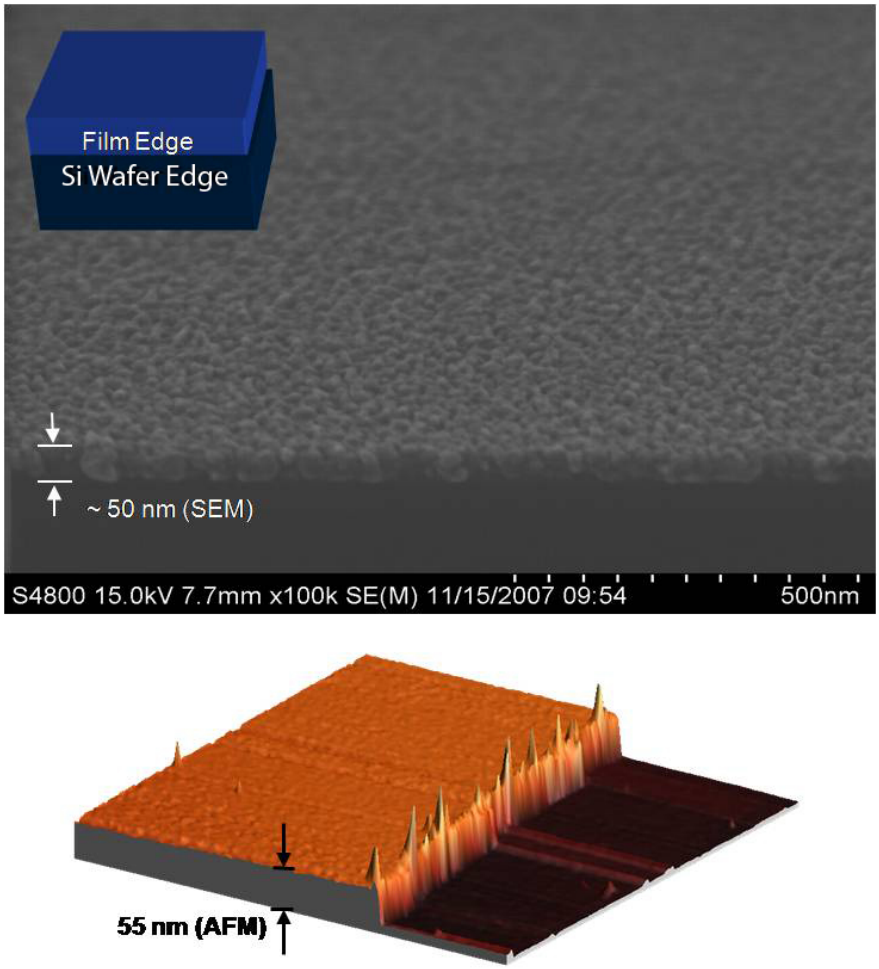

Figure 3.9. FESEM image (top) of SSF162 on a cleaved Si wafer showing side view of metal-dielectric film, and an AFM image (bottom) of SSF162 on glass near a scratch. For FESEM, the sample normal is tilted by 15° from the e-beam axis. The FESEM inset shows the orientation of the film edge and Si wafer edge, to aid the eye. The AFM image shows height in the third dimension and a measured step height from a 30×30 μm scan.

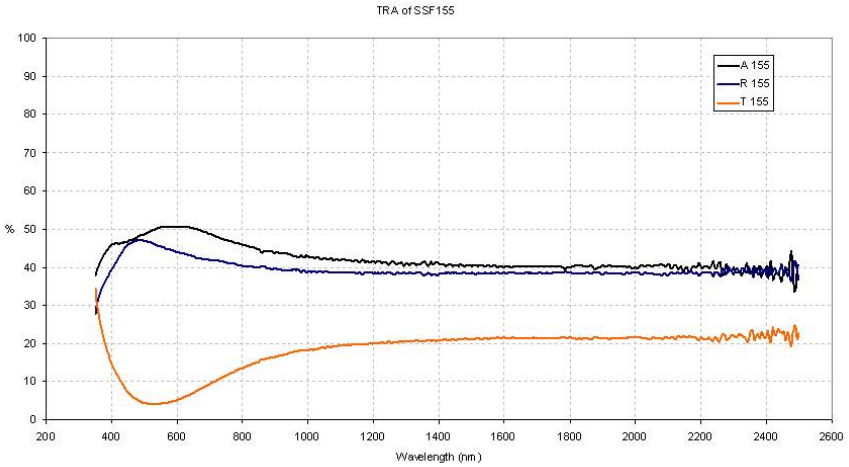

Figure 3.10. T/R/A spectra of SSF155. This is the reference film for all other sets and parameter variations. The film shows very strong absorption (A) throughout the range, with no discernable decrease in A as the wavelength approaches 2500 nm. Transmittance (T) is relatively low at $\sim$20% throughout the wavelength range, while A and reflectance (R) are about equal at $\sim$40% beyond 1200 nm. Together, the spectra indicate a film near the percolation threshold.

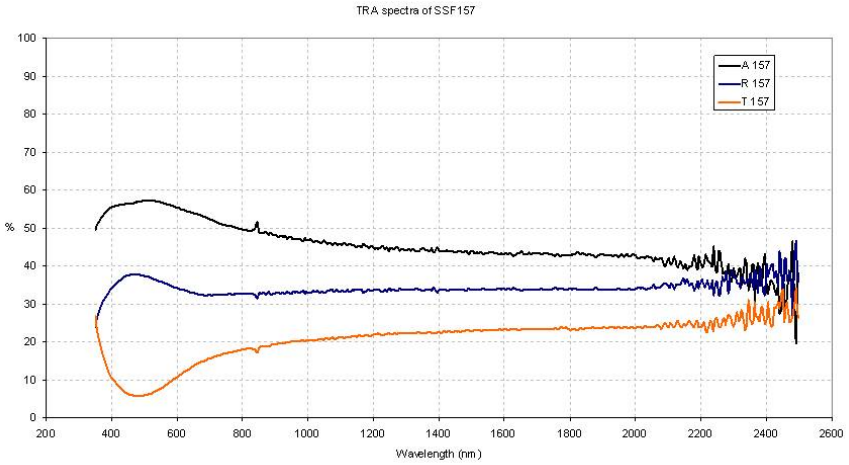

Figure 3.11. T/R/A spectra of SSF157. In this sample, A is similar to that of SSF155, even though the same metal content has been distributed throughout the film thickness more evenly in SSF157. The increase in A at the shorter wavelengths is indicative of more single-particle resonances in the film, which is also confirmed by FESEM images.

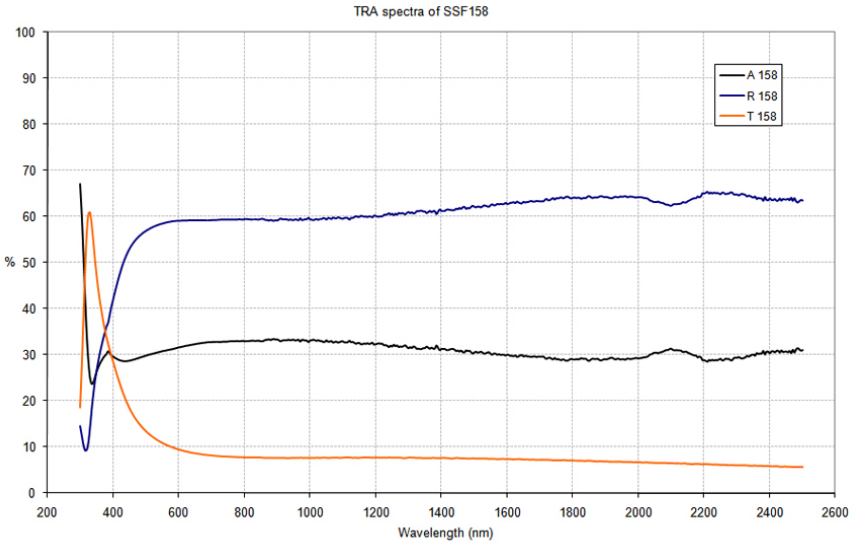

Figure 3.12. T/R/A spectra of SSF158, a two-metal-layer film with 12-nm Ag layers. Predictably, the film shows rather low T and relatively high R, but the A is flat at about 30% for most of the range. The individual metal layers are close to percolation, and the two of them act to absorb strongly in a wide wavelength range.

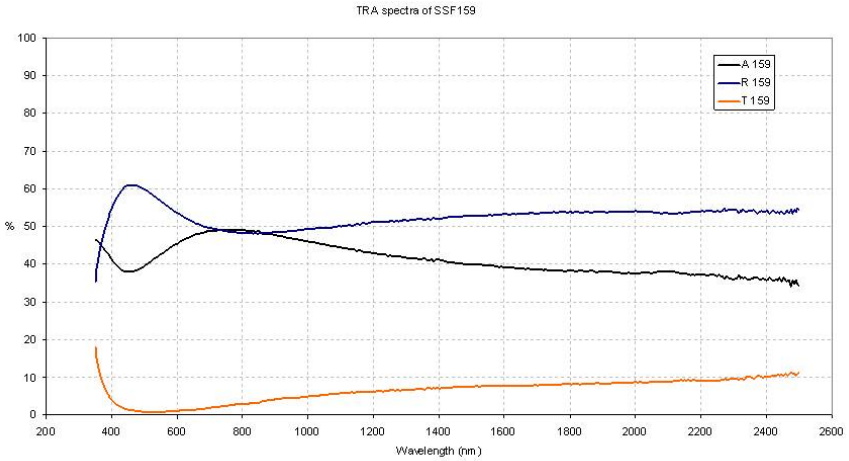

Figure 3.13. T/R/A spectra of SSF159, a film with high metal content, showing decreased T but about 60% R, which is strange considering it looks mirror-like in reflection. Notably, A is almost the same as other films, and T increases with λ.

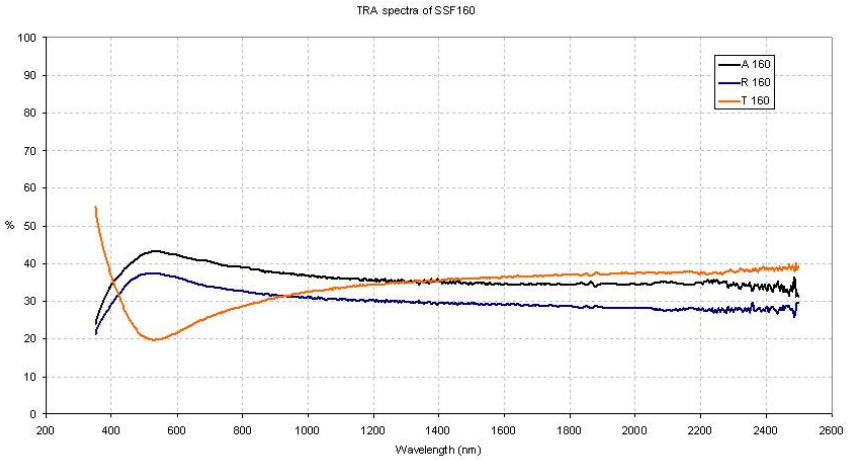

Figure 3.14. T/R/A spectra of SSF160 showing strong broadband A $\sim$ T $\sim$ R even out to wavelengths as long as 2500 nm.

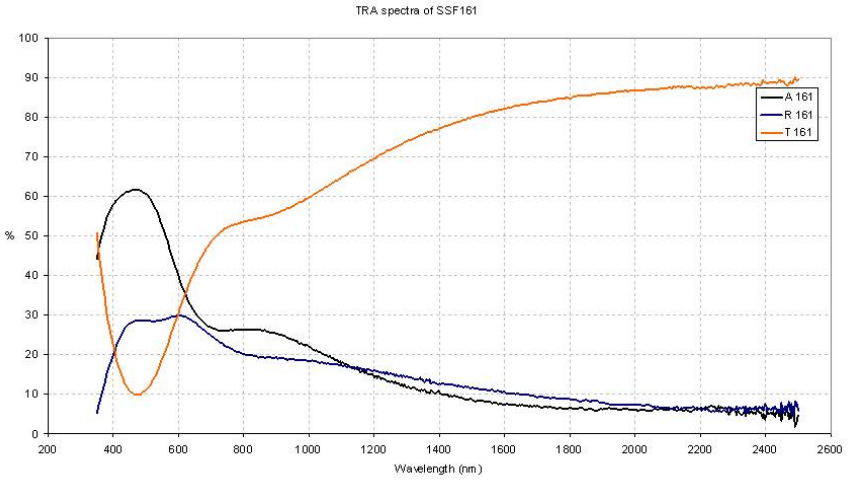

Figure 3.15. T/R/A spectra of SSF161 showing very high T at longer wavelengths, while A and R decrease to <10% for longer wavelengths. This is indicative of predominantly single-particle resonances in the film structure, which corresponds to the FESEM image of the sample.

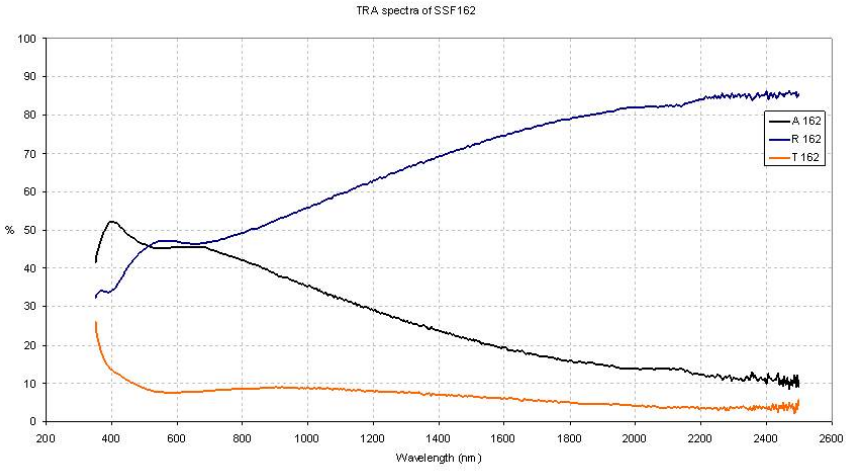

Figure 3.16. T/R/A spectra of SSF162 showing very low T (<10%) across the visible and NIR range. The R shows a minimum near 400 nm, corresponding to single-particle absorption in a dielectric, and A shows a corresponding maximum.

Chapter 4

Computational Analysis of Fabricated and Simulated Semicontinuous Films

The vast majority of the work directly funded by the Sandia-spoonsored fellowship has been in the experimental realm, fabricating and characterizing samples for use in various projects. However, computational simulations are an important complement to our experimental results and are a crucial method of efficiently planning new experiments. This chapter is therefore related to the computational analysis and simulation of metal-dielectric semicontinuous and composite film samples at Purdue. We begin with a description of the simulations based on effective medium theory formalisms. In Section 4, we discuss in detail how effective medium techniques have been used to simulate the operation of a composite NFSL superlens. We then discuss some of our recent full-wave, finite-difference time-domain (FDTD) simulations for 2D semicontinuous metal films. In the final sections, we describe some preliminary results from 3D FDTD simulations and give a look forward to the next steps in the simulations of true metal-dielectric composites.

Effective Medium Analysis of Metal-Dielectric Films

We have already mentioned that 2D semicontinuous films (or even 3D composite films) can be characterized by effective material parameters calculated using effective medium theory. We previously attempted to retrieve the effective parameters and obtain predicted reflectance and transmittance data for some of the metal-dielectric films we fabricated (the films were discussed in Section 3). Using EMT methods and fabrication data, the computational analysis calculated the effective material parameters the films and then retrieved predicted spectra data from those material parameters. Then, the predicted spectra were compared to the actual, measured spectra of the films. Unfortunately, only some of the sample spectra were successfully matched, with the others showing non-physical results in the predicted spectra. The codes had been vetted previously, so we were led to the conclusion that the EMT methods used to obtain the effective material parameters of the films were not accounting for all effects and phenomena present in the actual samples. This is a known shortfall of EMT, in that it does not account for interactions between inclusions within a system. For pure dielectric samples this is not typically a problem, but for metal inclusions the interactions between particles can have drastic effects on the overall system response. Hence, we decided to use more accurate finite-difference time-domain (FDTD) or full-wave simulations in order to simulate and retrieve effective parameters from our samples. However, methods such as

FDTD require a detailed knowledge of the exact geometry of the constituents materials in a metal-dielectric film. Obtaining that information precisely from fabricated films is essentially impossible for 3D films, but is readily available from SEM or TEM images for 2D films.

Simulations of Composite Superlens Field Translation

Our recent paper [63] has shown that it is feasible to use a composite near-field superlens to translate an enhanced field region from one side of the lens to the other, albeit with a lower translated amplitude. Previous sections of this document have mentioned this result in passing, and here we describe in more detail these important simulations. Using finite-element analysis and effective-medium techniques, we showed that the hot spots produced by a periodic array of silver nanoantennas can be spatially translated to the other side of a metal-dielectric composite superlens. This method of enhanced field translation enables surface-enhanced optical spectroscopy without the undesirable contact of molecules with metal, thus broadening the potential applications of sensing based on field-enhanced fluorescence and surface-enhanced Raman scattering.

The electric field-intensity enhancement (FE) along the center line of the unit cell is plotted in Figure 4.1(a). The superlens material is located between z=0 nm and z=.40 nm, while the nanoantenna elements are between z=20 nm and z=40 nm. At the bottom interface, the simulations show clearly that the FE peak occurs at an incident wavelength of 1100 nm. The FE along the center line at 1100 nm is plotted separately in Figure 4.1(c). At the bottom interface, the FE is around 226. The same nanoantenna array without the superlens was also simulated; the FE in this case is plotted in Figure 4.1(b) for comparison. In this case, the nanoantenna produces a hot spot at a wavelength of about 1160 nm. However, the hot spot in this case is confined inside the gap, and the enhanced fields vanish completely only a few nanometers away from the gap, which is evident in Figure 4.1(d). Comparing these two cases (with and without the superlens), we conclude that the field enhancement at the bottom interface is indeed the result of the superlensing effect, which enables the translation of enhanced hot spot fields from the top surface to the bottom surface. Note that the presence of the superlens shifts the resonant wavelength of the nanoantenna from 1160 to 1100 nm.

Hence, we have shown that by using a thin silver-silica composite layer as a near-field superlens, we can translate the hot spots generated by silver nanoantenna arrays to the other side of the superlens and thus move the hot spots away from the interface with metal. This opens the door for performing surface-enhanced detection away from the metal surface that produces the field enhancement, and may be of benefit to biosensing in particular where conformational changes due to metal surface interactions are often a concern.

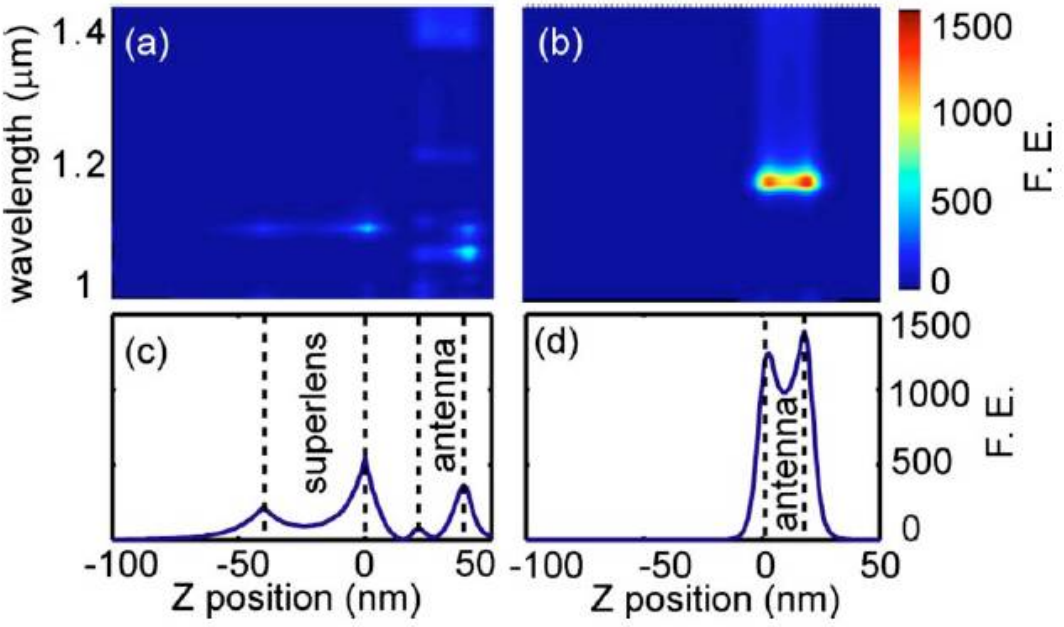

Figure 4.1. Computational results showing that a composite silver-silica superlens (0.71 metal volume ratio) can translate the enhanced fields from a silver nanoantenna pair to the far side of the lens. (a) The field enhancement (FE) along the center line of a unit cell; (b) the FE along the center line of a nanoantenna without the superlens; (c) the FE along the center line at a wavelength of 1100 nm with the superlens; (d) the FE along the center line at a wavelength of 1160 nm without the superlens. From [63]

Full-Wave Simulations of 2D Silver Films

In other previous simulations, we considered the spectral response from a semicontinuous silver film over a certain frequency range. This analysis technique is particularly interesting for us, as it gives us a way of obtaining full electromagnetic responses from a metal-dielectric structure, albeit in 2D. This process is briefly outlined here, and in the next section we discuss extensions of his technique to the third dimension in order to simulate 3D structures.

The crucial point of the 2D calculations presented here is that the geometries that were simulated are derived from real samples. Using actual SEM images from a sample, the simulations involved full-wave (finite-difference time domain, FDTD) calculations to obtain the electrodynamic response from a region of a sample assuming a 2D geometry (see Figure 4.2. Then, the electromagnetic field results were used to calculate the transmittance, reflectance and absorption spectra of the film. This process was repeated for several sections of one SEM image, and over several SEM images of the same sample, providing a number of realizations of the film's nanostructure. The various simulation results were then averaged and compared to the measured spectral response of the sample. An examples of the simulated and experimental spectra are shown in Figure 4.3, where we have calculated the reflection spectra of a film using this method and compared it to experimental results. The average simulated spectral response (solid line) agrees more strongly with the experimental result (dashed line) as more and more realizations of the film (light solid lines) are included in the average. In the results shown here, the simulated spectra are averages of at least eight realizations.

Full-Wave Simulations of 3D Metal-Dielectric Composite Films

One of the major goals of our recent research has been to extend the full-wave simulations mentioned above to additional samples, and to consider samples that are inherently three-dimensional in nature. One simplistic way of extending these simulations into three-dimensional films is to stack several SEM images representing 2D layers of a composite film into a 3D structure and then calculate the field distributions from the entire stackup. Although crude, this model provides some insight into the coupling between adjacent layers of a composite, multilayer film and the response of an entire 3D structure. Our group has been working to extend the full-wave simulation code to handle these additional requirements, but we have been hampered by changes in Purdue to the computational cluster systems and personnel changes within our group. However, we expect preliminary results soon on 3D full-wave simulations of MDC films.

Other methods of obtaining a simulated 3D morphology are also being pursued, including an analysis of growth models for island films on amorphous substrates. We are assessing these models to determine if they are suitable for simulating the actual deposition process seen in film fabrication. If these models are reasonable, we will develop tools to simulate the growth of composite metal-dielectric films in order to obtain morphologies that can be analyzed using FDTD calculations. These simulated samples and their calculated responses can then be used to guide the

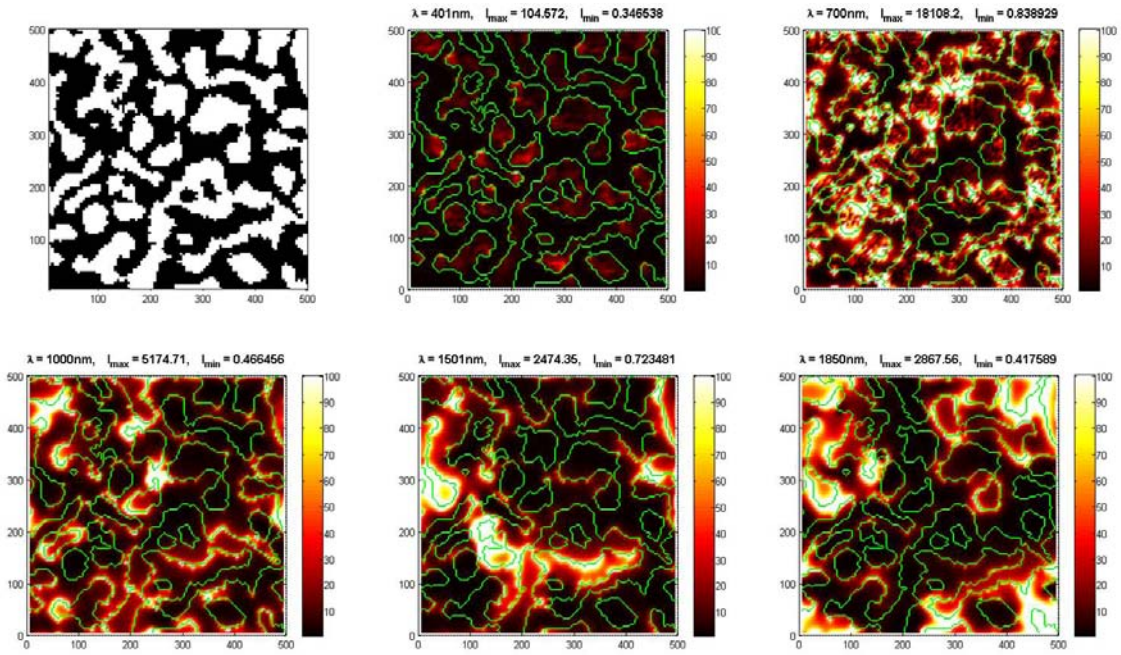

Figure 4.2. FDTD simulations show the field intensity near a semicontinuous silver film for different incident frequencies. The upper left panel shows the binarized SEM image of the actual sample used to calculate the electromagnetic response via FDTD methods. Each subsequent panel shows the field intensity at a particular wavelength: (l-r) 401 nm (I_{max} = 104.57, I_{min} = 0.35), 700 nm (18108.20, 0.84), 1000 nm (5174.71, 0.47), 1501 nm (2474.35, 0.72), 1850 nm (2867.56, 0.42)

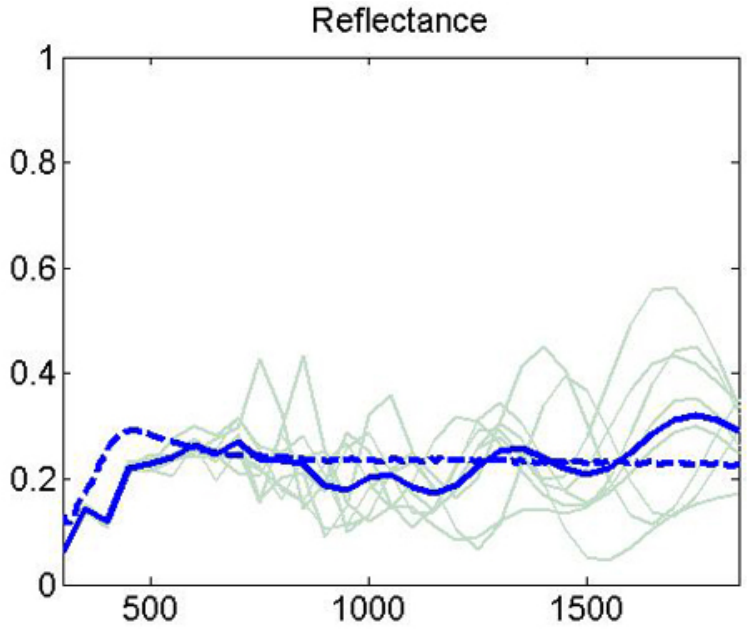

Figure 4.3. Simulations of a single-layer Ag film reflection response using several realizations of the film obtained via SEM images and calculated via FDTD. The solid line is the average of many realizations (faded lines). The dashed line is the experimental result.

fabrication of real samples for use as tunable near-field superlenses or other projects.

Chapter 5

Conclusions and Summary

In this work we have reviewed the research results sponsored in part by Sandia National Laboratories through the Purdue Excellence in Science and Engineering Fellowship program. The research, performed by Mark Thoreson (the fellowship recipient) and colleagues at the Birck Nanotechnology Center, encompassed studies on metal-dielectric plasmonic structures for a variety of applications.

We reviewed research on semicontinuous single-layer metal films and their applications in various kinds of enhanced biosensing, including surface-enhanced Raman scattering (SERS) spectroscopy. Our results show that the metal-dielectric SERS substrates we have created and studied actually show some very useful features in SERS sensing. Chief among these features is the adaptation of the metal nanoparticle structure of the substrates during biomolecule solution deposition. This adaptation acts to create a final structure that is very well-suited for electromagnetic field enhancement and SERS.

For our work on more complex samples, we reviewed our research on multilayer structures. These were broken into two overlapping categories: samples with distinct layers in cross-sectional views and those with indictinct layers. We have found that multilayer SERS-active samples show improved performance over single-layer SERS films, due to image charge coupling and long-range effects in a bulk silver sublayer included below the typical SERS layer and spaced a few nanometers away from the semicontinuous SERS-active layer.

Our multilayer strctures with indistinct layers are particularly interesting, with applications as exotic as superlensing and futher improvements to biosensing. Our work on these structures is also reviewed in this document, and we have shown that these samples, while difficult to fabricate repeatably and with predetermined properties, show promise as tunable near-field superlenses for the visible and near-IR wavelength ranges.

Finally, we reviewed our results on the computation and simulation research related to metal-dielectric composites. We have shown marked progress in these areas, with some exciting simulation experiments on 2D semicontinuous metal films and preliminary results on 3D random metal-dielectric composites (structures with indistinct layers). In our 2D film simulations, we have shown that it is possible to develop full-wave (finite-difference time domain) techniques based on real scanning electron microscope (SEM) images of a sample's metal nanostructure, and to approximate a sample's far-field and near-field responses using a number of averaged responses calculated from a pool of SEM images. We have begun working on extending this technique to 3D compos-

ite structures as a straightforward way in which to obtain more reliable predictions of a sample's response. Our previous methods, based partly on effective medium approximations for the metal-dielectric composiste permittivity, failed to take into account the possible interactions between metal particles and hence provided unreliable computational results in certain circumstances. The new simulation techniques do not suffer from these issues, but they are more complicated and computationally intensive to perform.

Overall, we have shown the wide range of studies completed as part of the Purdue Excellence in Science and Engineering Fellowship sponsored by Sandia National Laboratories. The research results will be of benefit to other scientists working in the areas of metal-enhanced biosensing, metamaterials and superlenses, and computational simulations of such systems. Hence, this fellowship program has helped to further the understanding of complex, composite, plasmonic systems and their applications. It has also helped to educate not only the fellowship recipient, but it has impacted many colleagues and coworkers who have interacted with the recipient on collaborations, scientific discussions and joint projects.

In addition to the Sandia National Laboratories sponsorship of this research through the Purdue Excellence in Science and Engineering Graduate Fellowship, this work was also sponsored in part by a grant from Inproteo, LLC; NSF grant HRD-0317722; NASA grant NCC-31035; the Edgewood Chemical Biological Center under the auspices of the US Army Research Office Scientific Services Program administered by Battelle (Delivery Order 0030, Contract No. W911NF-07-D-0001); ARO-STTR Grant No. W911NF-07-C-0008; and ARO-MURI Grant No. 50342-PHMUR.

References

[1] Tuan Vo-Dinh, Zygmunt Gryczynski, and Joseph R. Lakowicz, editors. *Plasmonics In Biology And Medicine (Proceedings of SPIE)*. SPIE-International Society for Optical Engineering, 2004.

[2] Christopher Loo, Amanda Lowery, Naomi Halas, Jennifer West, and Rebekah Drezek. Immunotargeted nanoshells for integrated cancer imaging and therapy. *Nano Letters*, 5:709–711, 2005.

[3] D. Patrick O'Neal, Leon R. Hirsch, Naomi J. Halas, J. Donald Payne, and Jennifer L. West. Photo-thermal tumor ablation in mice using near infrared-absorbing nanoparticles. *Cancer Letters*, 109:171–176, 2004.

[4] S. Pillai, K. R. Catchpole, T. Trupke, and M. A. Green. Surface plasmon enhanced silicon solar cells. *J. Appl. Phys.*, 101(9):093105–093105, 2007.

[5] Harry A. Atwater. The promise of plasmonics. *Scientific American*, pages 56–63, April 2007.

[6] H. Ritchie. Plasmon losses by fast electrons in thin films. *Physical Review*, 106:874–881, 1957.

[7] P.B. Johnson and R.W. Christy. Optical constants of the noble metals. *Phys. Rev. B*, 6:4370–4379, Dec 1972.

[8] E. D. Palik, editor. *Handbook of Optical Constants of Solids*, volume 1-5. Academic Press, 1997.

[9] Paul Drude. Zur elektronentheorie der metalle. *Annalen der Physik*, 1:566–613, 1900.

[10] Paul Drude. Zur elektronentheorie der metalle. *Annalen der Physik*, 3:369–402, 1900.

[11] Paul Drude. Zur elektronentheorie der metalle. *Annalen der Physik*, 7:687–692, 1902.

[12] Z. Wang, Z. Cai, Q. Chen, and L. Li. Optical properties of metal-dielectric multilayers in the near uv region. *Vacuum*, 80:438–443, 2006.

[13] Anatoliy Pinchuk, Gero von Plessen, and Uwe Kreibig. Influence of interband electronic transitions on the optical absorption in metallic nanoparticles. *J. Phys. D: Appl. Phys.*, 37:3133 – 3139, 2004.

[14] Vladimir P. Drachev, Uday K. Chettiar, Alexander V. Kildishev, Hsiao-Kuan Yuan, and Vladimir M. Shalalev. The Ag dielectric function in plasmonic metamaterials. *Optics Express*, 16(2):1186–1195, 2008.

[15] A. Vial, A.-S. Grimault, D. Macías, D. Barchiesi, and M. L. de la Chappelle. Improved analytical fit of gold dispersion: application to the modeling of extinction spectra with a finite-difference time-domain method. *Physical Review B*, 71:085416, 2005.

[16] www.nanohub.org, Accessed 2009.

[17] Xingjie Ni, Zhengtong Liu, and Alexander V. Kildishev. Photonicsdb: Optical constants, Feb 2008.

[18] Stefan A. Maier. *Plasmonics: Fundamentals and Applications*. Springer, May 2007.

[19] C. Bohren and D. Huffman. *Absorption and Scattering of Light by Small Particles*. Wiley-Interscience, 1983.

[20] Vladimir M. Shalaev. *Optical Properties of Nanostructured Random Media (Topics in Applied Physics)*, volume 82. Springer Verlag, Berlin Heidelberg, 2002.

[21] Hienz Raether. *Surface Plasmons on Smooth and Rough Surfaces and on Gratings*. Springer-Verlag, 1988.

[22] Uwe Kreibig and Michael Vollmer. *Optical Properties of Metal Clusters*. Springer, July 1995.

[23] Max Born and Emil Wolf. *Principles of Optics: Electromagnetic Theory of Propagation, Interference and Diffraction of Light*. Cambridge University Press, 7th edition, Oct. 1999.

[24] Charles Kittel. *Introduction to Solid State Physics*. John Wiley & Sons, Hoboken, NJ, 8th edition, 1996.

[25] J. Homola. *Surface Plasmon Resonance Based Sensors*. Springer-Verlag, Berlin, 2006.

[26] D. Stauffer. *Introduction to Percolation Theory*. Taylor and Francis, London and Philadelphia, 1985.

[27] K. Seal, M. A. Nelson, Z. C. Ying, D. A. Genov, A. K. Sarychev, and V. M. Shalaev. Growth, morphology, and optical and electrical properties of semicontinuous metallic films. *Phys. Rev. B*, 67:035318, 2003.

[28] Vladimir M. Shalaev. *Nonlinear Optics of Random Media: Fractal Composites and Metal-Dielectric Films (Springer Tracts in Modern Physics)*. Springer Tracts in Modern Physics). Springer, 1999.

[29] K. Seal, M.A. Nelson, Z. C. Ying, D.A. Genov, A.K. Sarychev, and V.M. Shalaev. Metal coverage dependence of local optical properties of semicontinuous metallic films. *J. Mod. Optics*, 49:2423–2435, 2002.

[30] Vladimir P. Drachev, Mark D. Thoreson, Vishal Nashine, Eldar N. Khaliullin, Dor Ben-Amotz, V. Jo Davisson, and Vladimir M. Shalaev. Adaptive silver films for surface-enhanced Raman spectroscopy of biomolecules. *Journal of Raman Spectroscopy*, 36:648–656, 2005.

[31] M. D. Thoreson. Semicontinuous metal-dielectric films: fabrication and characterization. Master's thesis, Purdue University, 2004.

[32] Milton Ohring. *The Materials Science of Thin Films*. Academic Press, 2 edition, 2001.

[33] D. B. Chrisey and Hubler G. K, editors. *Pulsed Laser Deposition of Thin Films*. John Wiley & Sons, 1994.

[34] T. J. Miller. Nano 101: a synopsis of resarch projects at Purdue University's Birck Nanotechnology Center. *Journal of Ultrapure Water*, In Preparation (2010).

[35] P. R. Griffiths and J. A. De Haseth. *Fourier Transform Infrared Spectroscopy*. Wiley-Interscience, 1986.

[36] P. Nyga, V. P. Drachev, M. D. Thoreson, and V. M. Shalaev. Mid-IR plasmonics and photomodification with ag films. *Applied Physics B*, 93(1 Sp. Iss.):59–68, 2008.

[37] Tuan Vo-Dinh, Leonardo R. Allain, and David L. Stokes. Cancer gene detection using surface-enhanced Raman scattering (SERS). *Journal of Raman Spectroscopy*, 33(7):511 – 516, 2002.

[38] Tuan Vo-Dinh. Surface-enhanced Raman spectroscopy using metallic nanostructures. *Trends in Analytical Chemistry*, 17(8-9):557–582, 1998.

[39] Dieter Zeisel, Volker Deckert, Renato Zenobi, and Tuan Vo-Dinh. Near-field surface-enhanced Raman spectroscopy of dye molecules adsorbed on silver island films. *Chemical Physics Letters*, 283(5-6):381–385, 1998.

[40] Tuan Vo-Dinh. SERS chemical sensors and biosensors: new tools for environmental and biological analysis. *Sensors and Actuators B: Chemical*, 29(1-3):183–189, 1995.

[41] Vladimir P. Drachev, Mark D. Thoreson, and Vladimir M. Shalaev. Sensing proteins with adaptive metal nanostructures. In Mark L. Brongersma and Pieter G. Kik, editors, *Surface Plasmon Nanophotonics*, Springer Series in Optical Sciences, chapter 14, pages 197–216. Springer, 2008.

[42] M. Moskovits. Surface-enhanced spectroscopy. *Rev. Mod. Phys.*, 57:783, 1985.

[43] V. P. Drachev, M. D. Thoreson, E. N. Khaliullin, V. Jo Davisson, and V. M. Shalaev. Surface-enhanced Raman difference between human insulin and insulin lispro detected with adaptive nanostructures. *J. Phys. Chem.*, 108(46):18046 – 18052, 2004.

[44] V.P. Drachev, M.D. Thoreson, E.N. Khaliullin, A.K. Sarychev, D. Zhang, D. Ben-Amotz, and V.M. Shalaev. Semicontinuous silver films for protein sensing. *Proc. of SPIE*, 5221:76–81, Nov 2003.

[45] V. P. Drachev, V. Nashine, M. D. Thoreson, D. Ben-Amotz, V. J. Davisson, and V. M. Shalaev. Adaptive silver films for detection of antibody-antigen binding. *Langmuir*, 21:8368–8373, 2005.

[46] E. N. Khaliullin. *Quantum size and nonlinear effects in metal nanostructures and bio-applications with SERS*. PhD thesis, Purdue University, 2005.

[47] D. A. Genov, A. K. Sarychev, and V. M. Shalaev. Metal-dielectric composite filters with controlled spectral windows of transparency. *J. Nonlinear Optics Physics & Materials*, 12(4):1–22, 2003.

[48] H. B. Liao, W. Wen, and G. K. L. Wong. Preparation and characterization of Au/SiO_2 multilayer composite films with nonspherical Au particles. *Applied Physics A: Materials Science and Processing*, 80:861–864, 2005.

[49] D. Babonneau, D. Lantiat, S. Camelio, J. Toudert, L. Simonot, and F. Pailloux. Gold and silver nanoparticles embedded in dielectric-capping layers studied by HAADF-STEM. *Eur. Phys. J. Appl. Phys.*, 44:3–9, 2008.

[50] J. Toudert, S. Camelio, C. Babonneau, M.-F. Denanot, T. Girardeau, J. P. Espi nos, and A. R. Gonzalez-Elipe. Morphology and surface-plasmon resonance of silver nanoparticles sandwiched between Si_3N_4 and BN layers. *J. Applied Physics*, 98:114316, 2005.

[51] B. Wood, J. B. Pendry, and D. P. Tsai. Directed subwavelength imaging using a layered metal-dielectric system. *Physical Review B*, 74:115116, 2006.

[52] Z. Jakšić, M. Maksimović, and M. Sarajlić. Silver-silica transparent metal structures as band-pass filters for the ultraviolet range. *Journal of Optics A: Pure and Applied Optics*, 72:51–55, 2005.

[53] M. D. Thoreson. *Metal-Dielectric Plasmonic Composites and Their Applicaitons*. PhD thesis, Purdue University, December 2009 (in preparation).

[54] R. C. Baetzold and J. F. Hamilton. Properties of small metal particles. *Prog. Solid St. Chem.*, 15:1–53, 1983.

[55] H. Brune. Microscopic view of epitaxial metal growth: nucleation and aggregation. *Surface Science Reports*, 316:121–229, 1998.

[56] Wenshan Cai, Dentcho A. Genov, and Vladimir M. Shalalev. Superlens based on metal-dielectric composites. *Physical Review B*, 72:193101, 2005.

[57] Nicholas Fang, Hyesog Lee, Cheng Sun, and Xiang Zhang. Sub-diffraction-limited optical imaging with a silver superlens. *Science*, 308:534–537, 2005.

[58] David O. S. Melville and Richard J. Blaikie. Super-resolution imaging through a planar silver layer. *Optics Express*, 13(6):2127–2134, 2005.

[59] Lihong Shi, Lei Gao, Sailing He, and Baowen Li. Superlens from metal-dielectric composites of nonspherical particles. *Physical Review B*, 76:045116, 2007.

[60] J. B. Pendry. Negative refraction makes a perfect lens. *Phys. Rev. Lett.*, 85(18):3966–3969, 2000.

[61] A. Röseler and E.-H. Korte. The optical constants of metallic island films used for surface enhanced infrared absorption. *Thin Solid Films*, 313-314:732–736, 1998.

[62] V. M. Shalaev and M. Moskovits, editors. *Nanostructured Materials: Clusters, Composites and Thin Films*, volume 679 of *ACS Symposium Series*. ACS Books, 1997.

[63] Z. Liu, M. D. Thoreson, A. V. Kildishev, and V. M. Shalaev. Translation of nanoantenna hot spots by a metal-dielectric composite superlens. *Applied Physics Letters*, 95:033114, 2009.

[64] D. A. G. Bruggeman. Berechnung verschiedener physikalischer konstanten von heterogenen substanzen. i. dielektrizitätskonstanten und leitfähigkeiten der mischkörper aus isotropen substanzen. *Ann. Phys.*, 24:636, 1935.

[65] A. Lakhtakia, editor. *Selected Papers on Linear Optical Composite Materials*. SPIE, Bellingham, WA, 1996).

[66] T. C. Choy. *Effective Medium Theory*. Oxford Science Publications, 1999.

[67] I. Horcas, R. Fernandez, J. M. Gomez-Rodriguez, J. Colchero, J. Gomez-Herrero, and A. M. Baro. Wsxm: A software for scanning probe microscopy and a tool for nanotechnology. *Rev. Sci. Instrum.*, 78:013705, 2007.

[68] V.P. Drachev, S.V. Perminov, S.G. Rautian, and V.P. Safonov. *Optical properties of nanostructured random media*, volume 82 of *Topics in Applied Physics*, chapter Nonlinear optical effects and selective photomodification of silver colloidal aggregates. Springer Verlag, Berlin Heidelberg, 2002.

DISTRIBUTION:

1 Mark D. Thoreson
Birck Nanotechnology Center
Purdue University
1205 West State Street
West Lafayette, IN

1 Vladimir M. Shalaev
Birck Nanotechnology Center
Purdue University
1205 West State Street
West Lafayette, IN

1	MS 0531	Joe Polito, 09000
1	MS 1423	Greg Hebner, 01128
1	MS 1423	Michael Pack, 01128
1	MS 1415	Eric Shaner, 01123
1	MS 1082	Igal Brener, 01727
1	MS 1082	Willie Luk, 01725
1	MS 0188	D. Chavez, LDRD Office, 01011
1	MS 0899	Technical Library, 9536 (electronic)

Sandia National Laboratories